CFD investigation of blind-tee effects on flow mixing mechanism in subsea pipelines

Fenghui Han, Yuxiang Liu, Muk Chen Ong, Guang Yin, Wenhua Li & Zhe Wang

Published online: 06 Jul 2022.

Submit your article to this journal ⧉

Article views: 505

View related articles ⧉

View Crossmark data ⧉

Citing articles: 1 View citing articles ⧉

Taylor & Francis
Taylor & Francis Group

CFD investigation of blind-tee effects on flow mixing mechanism in subsea pipelines

Fenghui Han [a,b], Yuxiang Liu[a], Muk Chen Ong [c], Guang Yin [c], Wenhua Li[a,b] and Zhe Wang [a,b]

[a]Marine Engineering College, Dalian Maritime University, Dalian, People's Republic of China; [b]National Center for International Research of Subsea Engineering Technology and Equipment, Dalian Maritime University, Dalian, People's Republic of China; [c]Department of Mechanical and Structural Engineering and Materials Science, University of Stavanger, Stavanger, Norway

ABSTRACT

Blind tees are widely used in subsea pipelines to enhance the mixing conditions of oil and gas products, but their structural design still relies on experience. In this paper, a series of numerical investigations have been carried out on blind-tee pipes in order to develop an in-depth understanding of their mixing mechanism and clarify the effects of blind-tee structures on the pipe flow. Firstly, the three-dimensional flow conditions in a typical blind tee have been simulated under different Reynolds numbers to investigate the mixing mechanism. Two critical Reynolds numbers for the vortex generations in blind tees are determined in the laminar flow regime, and the fitting curves of blind-tee vorticity dissipations are obtained. Then, the geometrical parameters, including the radial size ϕ, axial length (BSL) and position of the blind section, are varied systematically to study their effects on the flow characteristics and mixing conditions. The results indicate that increasing ϕ and BSL in an appropriate range can strengthen the flow circulation and promote the fluid exchange. Finally, an optimal configuration is obtained, which can improve the mixing capacity of blind tee by 53% in terms of the volume average vorticity as compared to the typical structure.

Nomenclature

D	pipe diameter
d	distance from the exit of blind tee to the selected cross section
h	average grid size
p	static pressure
r	radial position
R	pipe radius
Re	Reynolds number
Re_{c1}	first critical Reynolds number
Re_{c2}	second critical Reynolds number
$\boldsymbol{S}$	symmetric part of the velocity gradient tensor
S	cross-sectional area
S_L	local swirl number
S_G	global swirl number
U_{bulk}	inlet bulk velocity
U_t	tangential velocity
$\boldsymbol{u}$	velocity vector

u	velocity component in x direction
v	velocity component in y direction
w	velocity component in z direction
β_1	first dissipation coefficient
β_2	second dissipation coefficient
ζ	cross-sectional average value of absolute axial vorticity
ζ_0	cross-sectional average value of absolute axial vorticity at the exit of blind section
η	Kolmogorov length scale
θ	angular position
λ	volume of blind section
ν	kinematic viscosity
ρ	fluid density
ϕ	radial size of blind section
$\boldsymbol{\Omega}$	anti-symmetric part of the velocity gradient tensor
Ω_{avg}	volume average vorticity

CONTACT Zhe Wang ✉ wang.zhe@dlmu.edu.cn, zhe.wang.work@gmail.com

Abbreviations

BSL   axial length of blind section
EC   eccentric blind section
MCN   maximum Courant number

1. Introduction

The subsea pipelines for oil and gas industry are not always straight. In order to meet different requirements of the spatial distributions and flow situations, various types of bends are used in these pipeline systems, such as the elbows (Venters et al., 2021), T-junctions (Sakowitz et al., 2014) and Y-junctions (Chacon et al., 2015). However, severe flow challenges such as the phase separations, erosions and depositions often occur in these bending structures. Therefore, many analytical, numerical and experimental investigations have been performed on the flow characteristics inside the elbows and tees (Kalpakli Vester et al., 2015; Liu et al., 2021; Norouzi & Biglari, 2013).

Compared to straight pipes, the bending structures often induce strong secondary flows superimposed on the main streams, which will greatly change the flow patterns and phase distributions in the pipelines. Dean and Chapman (1928) first studied the secondary flow pattern in bent channels, and proposed the Dean number. Since then, the secondary flow induced by elbows has attracted more and more attention. Nandakumar and Masliyah (1982) numerically analyzed the bifurcation of two-vortex and four-vortex secondary flows downstream of different elbow structures. Bovendeerd et al. (1987) used the laser-Doppler velocimetry to measure the secondary flow through a 90° bend in the laminar regime, and found the position of the maximum secondary velocity. To further reveal the flow mechanism in curved pipes, detailed structures of secondary flows have been investigated. Bhunia and Chen (2009) defined and analyzed the five types of secondary flow structures downstream of the pipe bends, including the base vortex, split base vortex and different types of Dean vortices. The Dean instability, as a sign of vortex switching, was studied downstream of an elbow using the snapshot proper orthogonal decomposition analysis by Hellström et al. (2013). According to the Dean instability analysis, Li et al. (2017) found new entrainment Dean vortices at the exit of the bent channel. The dissipation, separation and modeling strategy of the secondary flows were also investigated by Kim et al. (2014) and Dutta et al. (2016). Gholami et al. (2014) studied the secondary flow patterns in a strongly-curved 90° open channel bend experimentally and numerically. In addition to single-bend structures, flow measurements were also conducted to investigate the complex characteristics of secondary flow in elbow combinations (Ebara et al., 2016; Yuki et al., 2011). For the pipe junctions, Sakowitz et al. (2013) analyzed the secondary flow structure, mixing quality and flow mode in a T-junction with large eddy simulation, and indicated that the flow structures in the junctions were attributed to a Kelvin-Helmholtz instability. Georgiou and Papalexandris (2018) investigated the flow separation structures and the shear layer properties in T-junctions using a direct numerical simulation. Dianita et al. (2021) studied the effects of connection angle and diameter of T- and Y-shaped junctions on the flow performances.

In order to ensure the offshore oil and gas transportation in underwater production systems, a lot of research has been conducted on the challenges induced by multiphase flows in subsea pipelines. Many researchers have performed studies on gas–liquid two-phase flows, such as bubble flows (Ambrose et al., 2016; Özkan et al., 2015) and slug flows (Dai & Wang, 2014; Lv et al., 2020). Liu et al. (2019) investigated the effect of elbow flow configuration and hydrodynamic parameters on the corrosion-prone characteristics of elbow systems. For the solid–liquid flow, Vittorio Messa and & Malavasi (2014) presented a new two-fluid model for the numerical prediction of the distribution of the solids. Xu et al. (2020) studied the influence of the marine dynamic environment on the solid–liquid two-phase flow field in the pipeline and revealed a large disturbance of the transverse swing convection field on the pipelines.

As a special type of bending structures in subsea pipeline systems, blind tees are the key components in the technology of multiphase flow meters (Brister, 2013), which could provide good sampling conditions for multiphase flow measurements in submarine pipelines (Pinguet et al., 2012). Previous experimental research studies have proved that blind tees can improve the axis-symmetry of gas–liquid phase distribution and promote the mixing of multiphase fluids (Hjertaker et al., 2018; Rammohan et al., 2013; Razali et al., 2021). In addition, some researchers focused on the effect of blind tees on the erosion control of pipe bends. According to the research of Chen et al. (2006), the erosion magnitude of blind tee at high sand volume concentration was two orders less than that of the elbows. Pouraria et al. (2016) found that the erosion of blind tee was greatly related to the pipe geometry, fluid quality and velocity. Considering the important role of blind tees in the erosion control, fluid sampling and multiphase measurement, studies on the flow characteristics inside blind tees are quite essential. Ong et al. (2017) first analyzed the typical configurations of blind tees at a specified Reynolds number based on CFD simulations. Then, Han et al. (2020) simulated the

flow characteristics of blind tees at low Reynolds numbers, and discussed the effects of blind-tee length, end structure and inlet velocity on the internal flow of blind tees.

However, detailed flow mechanism of how the blind tees improve the flow mixing conditions has not been clearly revealed yet, especially for the development of the complex secondary flow induced by the blind section. In addition, since the effects of the structural parameters of blind tees have not been thoroughly investigated, the structural design of this important component still relies on experience, lacking a specific theoretical guidance. Although the Reynolds number used in the oil and gas industry commonly ranges from 10^2 to 10^6, for the pipeline transportations of acid crude oil and heavy oil, the Reynolds numbers are generally from 50 to 1500 (Keleşoğlu et al., 2012; Santos et al., 2017). The researchers also report that these fluids generally show the property of Newtonian fluid in the transport conditions (Bazyleva et al., 2010; Ilyin & Strelets, 2018). Therefore, in this paper, a three-dimensional numerical study has been carried out on the internal flow of blind tees in the Reynolds numbers ranging from 500 to 1500 with Newtonian fluid. The development of the secondary flow structures downstream of the blind tee is analyzed, and how the backflow from the blind section blends with the main flow is revealed. The geometrical parameters that define the blind-tee structures are also varied systematically to study their effects on the pipe flow characteristics and mixing conditions. This research is expected to develop an in-depth understanding of the flow mixing mechanism in blind tees, clarify the influence of their structures, and provide references for the optimal design of blind-tee pipes.

2. Methodology

2.1. Numerical method

In this study, the three-dimensional Navier-Stokes (N-S) equations have been employed to solve the single-phase laminar flow in different blind-tee configurations. Since the pipe flow is generally considered as incompressible, the N-S equations can be simplified as:

$$\nabla \cdot \boldsymbol{u} = 0 \tag{1}$$

$$\frac{\partial \boldsymbol{u}}{\partial t} + \boldsymbol{u} \cdot \nabla \boldsymbol{u} = -\frac{1}{\rho}\nabla p + v \cdot \Delta \boldsymbol{u} \tag{2}$$

where ρ represents the fluid density, v is the kinematic viscosity, p represents the static pressure and $\boldsymbol{u}$ is the fluid velocity vector.

ANSYS CFX is used as the solver for the numerical simulations with a time-implicit pressure-based coupling algorithm, a three-dimensional element-based finite volume method, and a high-resolution advection scheme. The calculations are regarded as convergence when the RMS residual is lower than 10^{-5}.

2.2. Computational domain and boundary conditions

Figure 1 shows the computational domain and grids for a typical blind tee analyzed in this paper. It includes a 20D straight inlet pipe, a blind section and a 30D straight pipe in the downstream, where D represents the pipe diameter. Structured grids are generated by ANSYS ICEM for all the computational configurations investigated in the present study.

In the numerical models, the inlet boundary condition is set as a full-developed laminar flow. According to the classical formula given by Cengel and Cimbala (2014), the velocity distribution of which is written as:

$$U(r) = 2U_{bulk}\left(1 - \frac{r^2}{R^2}\right) \tag{3}$$

where r is the radial position, R is the pipe radius, and U_{bulk} is the inlet bulk velocity which changes with the Reynolds number.

At the exit of the computational domain, the outlet pressure is set to be zero, and the velocity condition is zero normal gradient. All the solid walls of the tubes are modeled as nonslip walls.
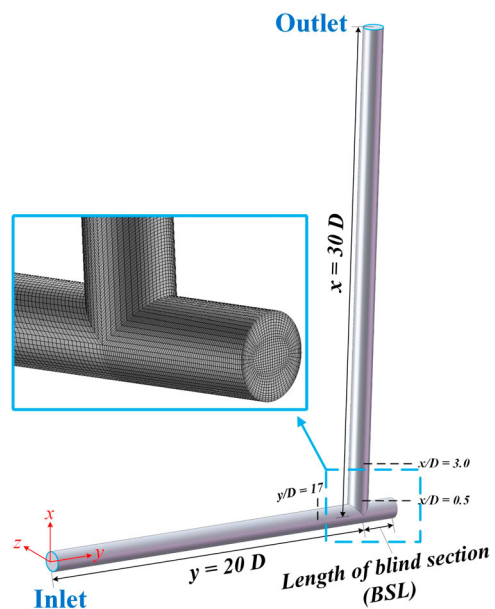

**Figure 1.** Computational domain and grids for a typical blind tee.

3. Verification and validation

In order to validate the numerical results obtained in this paper, grid convergence studies are carried out on all the computational models, and the reliability of the numerical method is also verified against the published experimental data.

The grid convergence study of the $2D$ blind section at $Re = 1000$ is provided here as an example. Four different computational grids have been generated for this configuration, and the cross-sectional velocity distributions at $y/D = 17$ and $x/D = 3$ in both the upstream and downstream of the blind section are compared in Figure 2(a). It shows that the cross-sectional velocity distributions at $y/D = 17$ in the inlet pipe have a good consistency in the four meshing strategies. At $x/D = 3$, the velocity profiles obtained by using Mesh 3 (757272 elements) and Mesh 4 (970952 elements) are quite close, the average and maximum velocity deviations of which are only 0.8% and 1.6%, respectively. However, compared with Mesh 3, when the grid resolution decreases to Mesh 2 (488120 elements) and Mesh 1 (245231 elements), the average velocity deviation increases to 6.2% and 9.7%, respectively, and the maximum velocity deviation increases to more than 15%. The corresponding velocity contours and vectors at $x/D = 3$ are shown in Figure 2(b), and the y^+ value defined as $u_\tau y_{wall}/\nu$ (where u_τ is the friction velocity, y_{wall} is the height of first layer grid and ν is the kinematic viscosity) obtained with Mesh 3 are displayed in Figure 2(c). It can be found that the high-speed regions near the outer side of the pipe and two pairs of counter rotating vortices are clearly captured by Mesh 3, and the corresponding y^+ values are less than 2, indicating a good grid resolution near the wall. According to the grid convergence study, Mesh 3 with 757272 elements is considered to have sufficient accuracy for the numerical simulation in this study.

In addition, the accuracy of the meshes can be further checked by the ratio of average grid size h (where h is defined as $\sqrt[3]{\Delta x \Delta y \Delta z}$ of each cell) to the Kolmogorov length scale $\eta = (\nu^3/\varepsilon)^{\frac{1}{4}}$, where $\nu = U_{bulk}D/Re$ and $\varepsilon \approx U_{bulk}^3/D$ (Kresta & Wood, 1993). Moser and Moin (1987) reported that most of the dissipations in curved channels occur at the scale greater than 15η, and Cao et al. (2020) also noted that the flow kinetic energy is dissipated in the scale of 10η. They pointed out the smallest scale must be resolved to capture sufficient flow details. For the simulations in the present study at different Reynolds numbers, it can be calculated that the ratio of h to η is in the range of 4.11–9.25 for the whole pipe, and h/η for the blind section is only 2.55–5.75, which meet the requirement of capturing the smallest scale. In addition, Komen et al. (2014) revealed that in terms of pipe flows, when
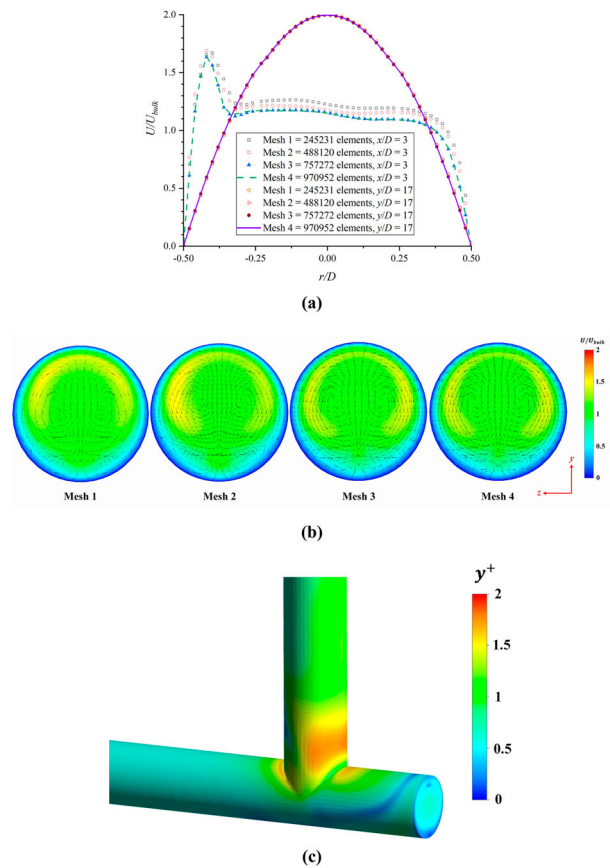
Figure 2. Comparisons of grid convergence study: (a) cross-sectional velocity profiles; (b) velocity contours and vectors at $x/D = 3$; (c) y^+ values obtained with Mesh 3.

the grid resolution is sufficient, the finite volume method can realize a quasi-direct numerical solution to obtain adequate results of the flow field, which is also used in this investigation. Based on the above consideration, it can be concluded that the present simulations can capture sufficient flow details in blind-tee pipes. Then, the time-step convergence study has been carried out for Mesh 3 with the maximum Courant numbers (MCN) of 0.2, 0.5 and 1. Figure 3 shows the result of the time-step convergence study at $x = 3D$, revealing that MCN = 0.5 is sufficiently accurate for the present simulations.

In order to validate the numerical method used in this study, the internal flow of a 90° elbow has been simulated to compare with the published experimental work of Bovendeerd et al. (1987), where the Reynold numbers of the pipe flow was 700. The corresponding computational domain and flow condition are modeled with the numerical method used in the present study, and the simulation results have been verified against the experiment data. Comparisons of the measured and predicted velocities have been made on different cross sections in the elbow. Figure 4 shows the numerical and experimental results
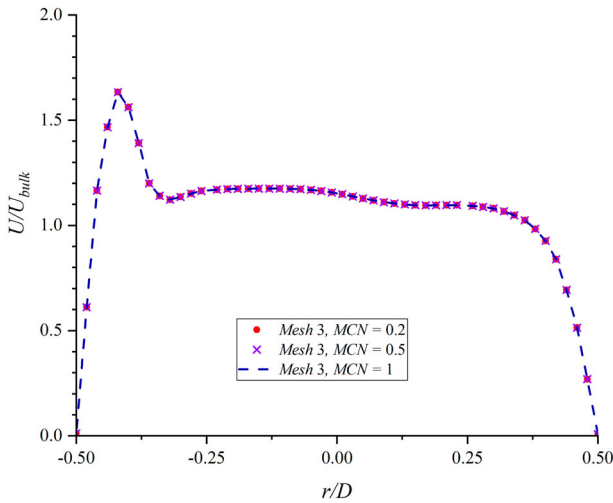
Figure 3. Comparisons of time-step convergence study at $x/D = 3$.

on the cross sections at $\theta = 39.8°$ and $81.9°$ of the bend using the variation of the dimensionless velocity U/U_{bulk} with the dimensionless radial position r/D. It can be found that the velocity profiles of the numerical results are in a good agreement with the experimental data at $\theta = 39.8°$ and $81.9°$. The corresponding average velocity deviations between the numerical and experimental values are 4.02% and 1.09%, respectively. In addition, the experimental data on all the seven cross sections measured by Bovendeerd et al. (1987) has been compared with the numerical results. It indicates that the average uncertainty of the numerical method used in the present study is 3.84%. In order to further validate the numerical accuracy, detailed comparisons between the velocity contours of the numerical and experimental results on the cross sections of $\theta = 39.8°$ and $81.9°$ are displayed together with the velocity profiles in Figure 4, and a good consistency can be found between the experiment data and the numerical results.

According to the validation study, the numerical method used in this paper is proved to be reliable for predicting the flow characteristics in bending structures, which will be utilized for the simulations of the typical and modified blind tees.

4. Results and discussions

4.1. Mixing mechanism in blind tees

In order to reveal the mixing mechanism in blind tees, the three-dimensional flow characteristics in a typical structure with blind-section length BSL = 2D has been thoroughly investigated in this section as the first step of this study, which will provide guidance for the structural modifications in the next section.

4.1.1. Blend of main flow and backflow

In this section, the blend of the main flow and the backflow from blind section has been discussed to have a preliminary understanding on the mixing condition inside the blind tee. For the beginning, the two-dimensional streamlines on the symmetrical plane and three-dimensional streamlines in this typical blind tee at $Re = 1000$ are shown in Figure 5, which provides an intuitive knowledge of the flow characteristics. The flow bifurcation can be found at the bend corner, where part of the fluid flows to the blind section and the rest directly turns to the downstream. Due to the blockage of the end wall, the fluid in the blind section is trapped, and a flow circulation is generated there. In addition, a flow separation region with the size of $1D$ forms near the inner side downstream of the blind tee.

As shown in Figure 6, the cross-sectional velocity distributions along the pipe downstream of the blind tee have been displayed and compared at five different locations (i.e. $x/D = 1.5, 2.5, 3.5, 5.5$ and 20.5). The velocity distributions show a strong nonuniformity when $x/D < 3.5$, and the flow speed near the outer side of the pipe is higher than that near the inner side. Two peaks and one valley are observed on the velocity profile in this region, and the maximum difference appears at $x/D = 1.5$. It implies that, for this specific case, the flow mixing process mainly exists in the range of $x/D < 3.5$. As the fluid continues to flow downstream, the velocity profile becomes uniform in the range of $3.5 \leq x/D \leq 5.5$, and finally gets close to the parabolic shape of the fully developed pipe flow at the outlet. Different from the velocity profile of traditional elbow flow with only one peak near the outer side (Bovendeerd et al., 1987; Lim & Chung, 1999), another velocity peak appears near the inner side in the downstream of the blind tee, which is induced by the blind section. Therefore, it could promote further mixing of the pipe flow, and provide a better condition for the flow sampling and measurements.

In order to further discuss the fluid transfer and mixing process in the blind-tee pipe, the flow details inside and downstream of the blind section have been investigated by means of the streamlines and velocity vectors in Figure 7. It is clearly observed that in Figure 7(a), due to the centrifugal force, the fully developed main flow from the inlet pipe turns 90° to the downstream along the outer side of the bending structure, which forms the peak velocity on the outer side of the downstream pipe. Then, part of the mainstream flows from the outer side to the inner side rapidly driven by the reverse pressure. Figure 7(b) displays the streamlines on the symmetric plane as well as the velocity vectors on two cross sections inside the blind tee (i.e. $y/D = 20.5$ and 21). It reveals that, when
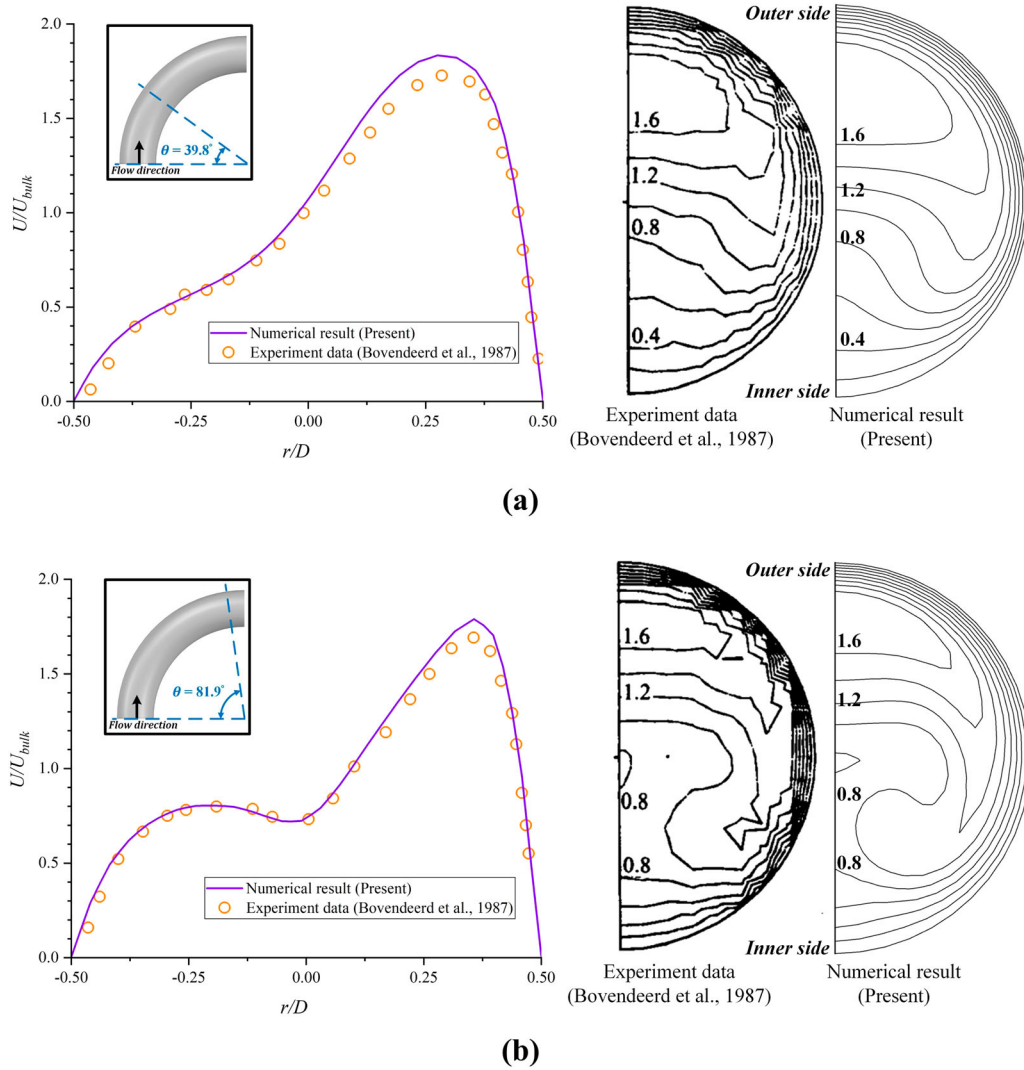
Figure 4. Velocity profiles and contours of validation study at (a) $\theta = 39.8°$ and (b) $\theta = 81.9°$ of the bend.
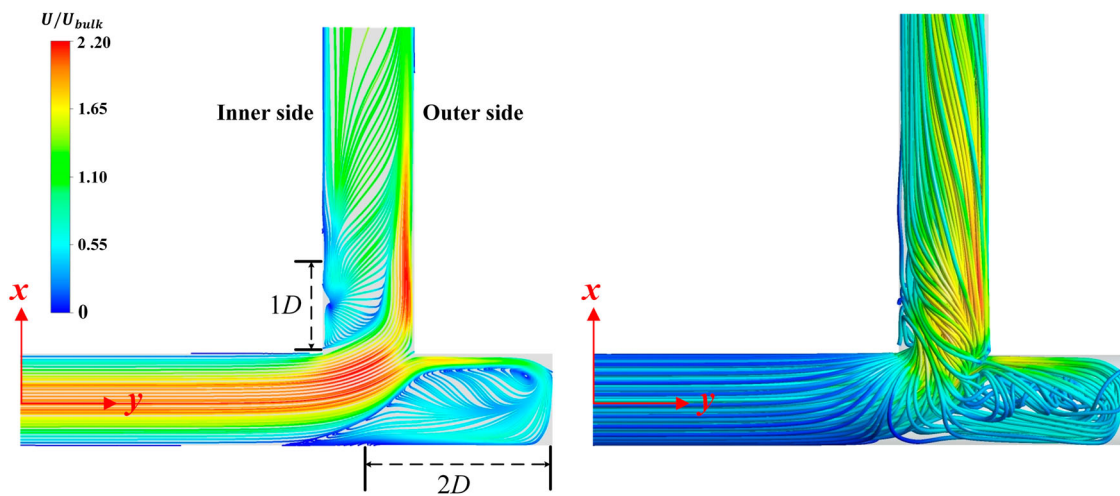
Figure 5. Two- and three-dimensional streamlines in typical blind tee at $Re = 1000$.
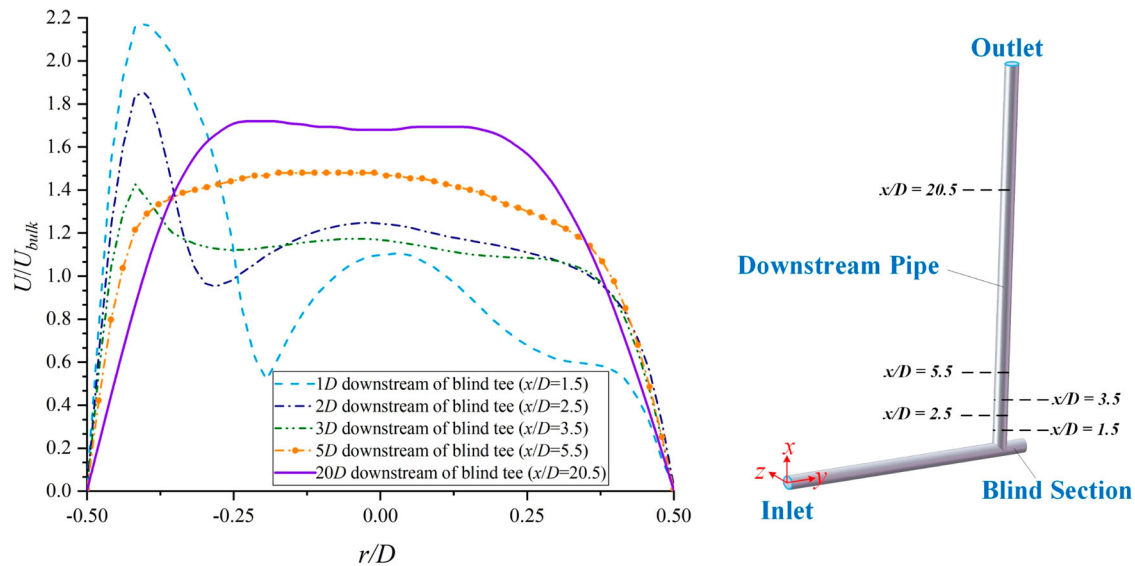
Figure 6. Velocity distributions at different locations downstream of typical blind tee at $Re = 1000$.

the fluid bifurcation appears at the bend corner, part of the high-speed fluid flows into the blind section, rushes to the dead end and forms great flow circulations. The three-dimensional velocity vectors in the blind section indicate that most of the backflow enters the dead end from the upper side, and finally flows out of the blind section along the lower side of the pipe. Therefore, the flow directions at the upper and lower sides of the blind section are opposite. The velocity vectors also reveals that a pair of counter rotating vortices is induced by the backflow, which can promote the fluid mixing in the blind section. In addition, the three-dimensional streamlines of the backflow including and excluding the upstream flow are shown in Figure 7(c), and the corresponding velocity vectors are added on the streamlines including the upstream flow (i.e. the left figure) to specify the development of the backflow. It can be observed in the left figure that the backflow enters the blind section from the upper side, generates flow circulations, and then flows out from the lower side, which is consistent with the above discussion. The streamlines with velocity vectors also indicate that, after flowing out of the blind section, the backflow enters the downstream pipe along the pipe wall at the bending corner. Subsequently, the backflow divides into two parts, i.e. the high-speed and low-speed backflows shown in the right figure. Due to the low pressure in the flow separation region near the inner side of the bending structure, the low-speed backflow is sucked into the inner corner of the downstream pipe, circulates into a pair of small vortices, and finally mixed with the main flow to the downstream. Meanwhile, the high-speed backflow directly meets the main flow at the entrance of the blind section, and then flows to the downstream with high velocities due to the energy and mass transfer

with the main flow in the mixing process, which might be the cause of the second velocity peak in the range of $x/D < 3.5$. Based on the above analysis, the mechanism and mixing process of the main flow and backflow are clearly illustrated, and it proves that the fluid mixing is enhanced in the blind-tee structure owing to the backflow from the blind section.

4.1.2. Development of secondary flow structures

It has been concluded by Jarrahi et al. (2010) that a more complex secondary flow yields a better transverse mixing. Therefore, in this section, the developments of secondary flow structures under different Reynolds numbers caused by different blind-tee configurations have been discussed. The length of blind section ranges from $1D$ to $3D$ (i.e. BSL $= 1D, 2D$ and $3D$), and the Reynolds number varies from 500 to 1500.

Figure 8 shows the streamlines for the secondary flow analysis on different sections downstream of the blind tee with BSL $= 2D$ at $Re = 1000$. The centrifugal force balances against the pressure gradient in the bending structure, and the high-speed fluid is forced to the outer side of the pipe because of the high centrifugal force. Meanwhile, the low-speed fluid near the pipe wall is forced inward due to the reverse pressure gradient. Therefore, a pair of counter rotating vortices forms and develops right after the bending structure (i.e. $x/D = 0.5, 0.8$ and 1), which is called the base vortices. As the distance increases to $x/D = 1.3$, two pairs of new vortices appear on the inner and outer sides, respectively. The outer-side vortices are known as the additional Dean vortex, which typically occurs in the bending structures with high curvature ratios (Dutta & Nandi, 2021). They shrink quickly in size and totally disappear at $x/D = 1.5$. The vortices
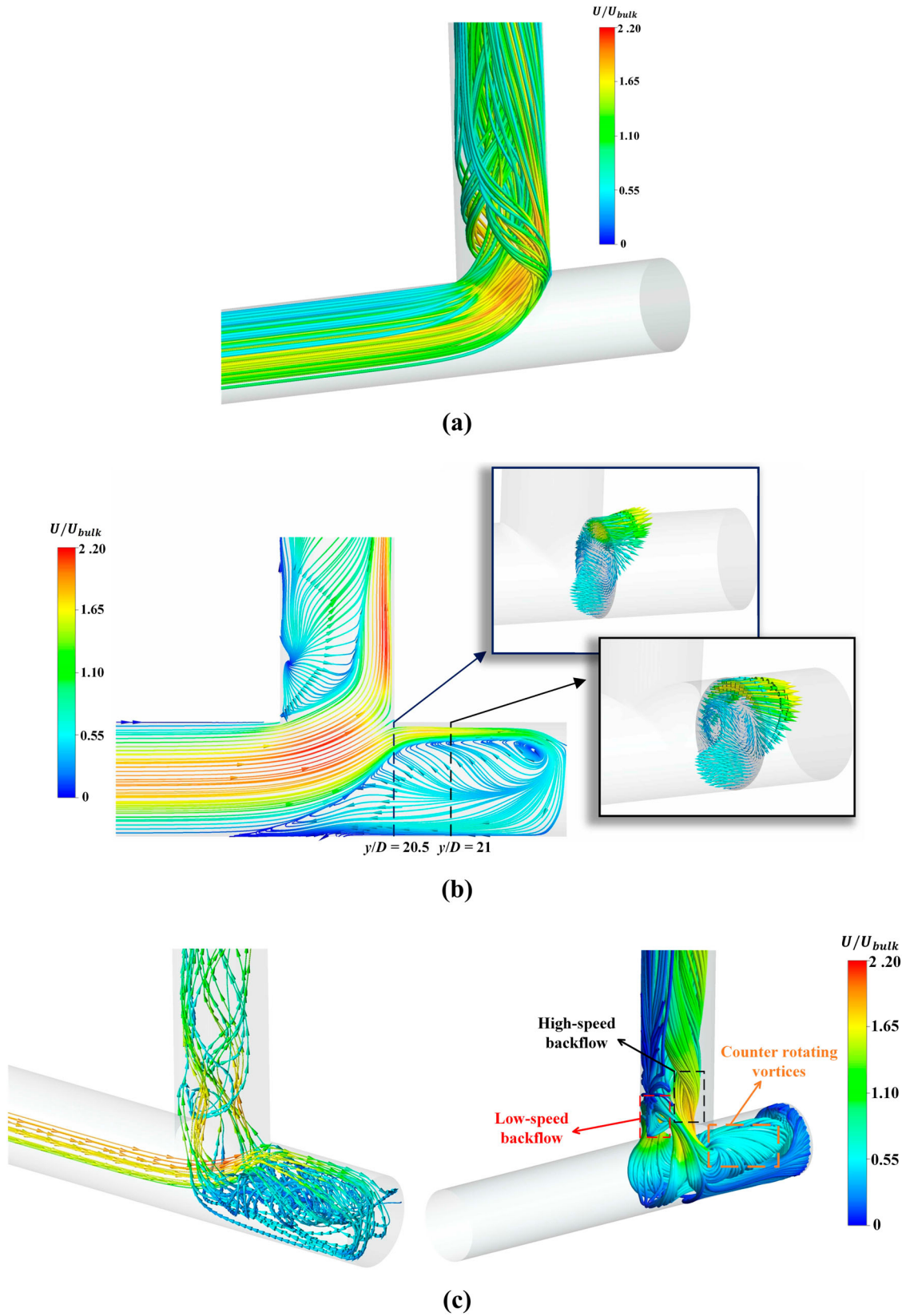
Figure 7. Main flow and backflow in blind tee: (a) Three-dimensional streamlines of main flow; (b) Streamlines on the symmetrical plane and velocity vectors in the blind section; (c) Three-dimensional streamlines of backflow including and excluding upstream flow.
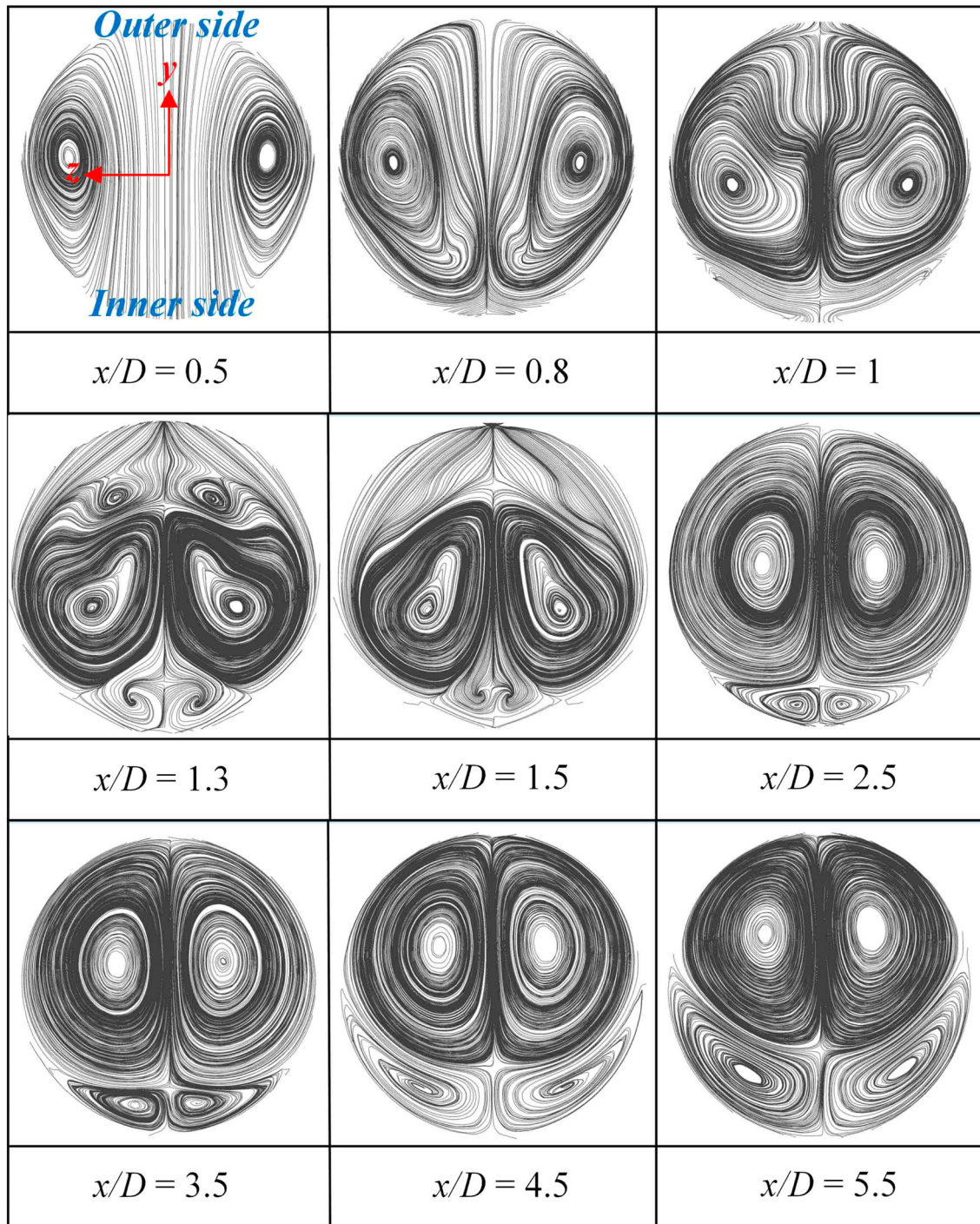
Figure 8. Streamlines on different sections downstream of blind tee with BSL $= 2D$ at $Re = 1000$.

on the inner side exist in the flow separation region and are affected by the reverse pressure gradient, which are similar to the inner corner Dean vortex (IC Dean vortex) defined by Bhunia and Chen (2009). However, the IC Dean vortex only appears in a very short distance with a small size in the traditional elbow (Pantokratoras, 2016), while the backflow from the blind section also contributes to the vortices in the separation region as discussed in the previous section. When x/D increases from

2.5 to 5.5, the vortices on the inner side still exist, mix with the base vortices, and gradually become larger. This explains why a uniform velocity profile is obtained at x/D = 5.5 in Figure 6.

In order to further investigate the characteristics of vortices downstream of the blind tee, the tangential velocity distributions at $x/D = 1.3$ are provided in Figure 9, including the tangential velocity contour and vectors as well as the tangential velocity profiles of the outer-side,
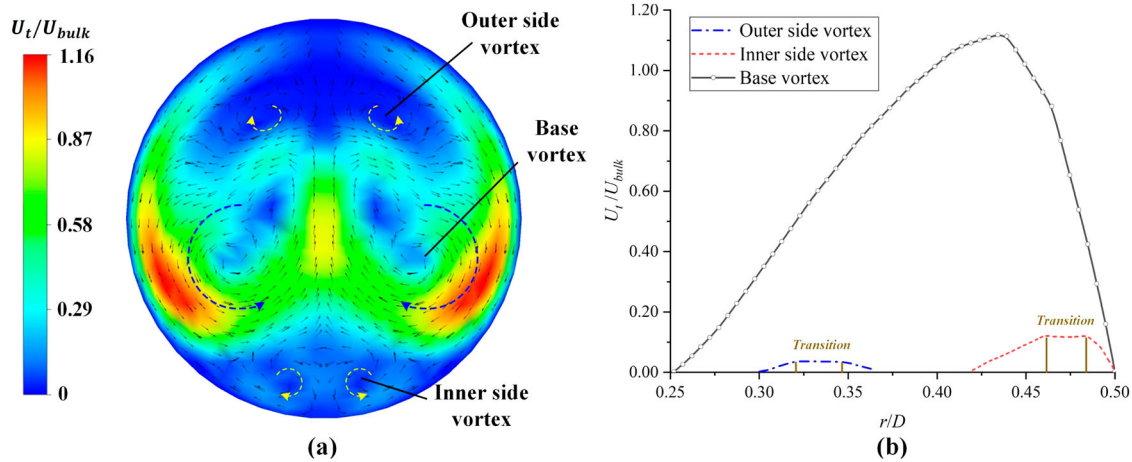
Figure 9. Tangential velocity distributions at $x/D = 1.3$ of the blind tee with $BSL = 2D$ at $Re = 1000$: (a) Tangential velocity contour and vectors; (b) Tangential velocity profiles of the outer-side, inner-side and base vortices.

inner-side and base vortices. For the tangential velocity profiles in Figure 9(b), the transverse axis represents the dimensionless radial position r/D from the vortex core to its boundary, and the vertical axis is the dimensionless tangential velocity U_t/U_{bulk}. The locations and rotational directions of the outer-side, inner-side and base vortices are clearly displayed in Figure 9(a). It is observed that the rotational direction of the base vortex is opposite to both the outer- and inner-side vortices, and the tangential velocity of the base vortex is much higher than that of the other vortices. In addition, the tangential velocity variations of these vortices are shown in Figure 9(b). It can be found that, with the increase of the radial position r/D, the tangential velocities of the three types of vortices grow linearly from the corresponding vortex core at first, characterized by a solid-body rotation. Then, the tangential velocity of the base vortex decreases rapidly after reaching the peak value, but a transition region appears in both the outer- and inner-side vortices, which is mainly induced by the influence of the base vortex with the opposite rotational direction. The behaviors of these vortices and their tangential velocity distributions lead to a result that the secondary flow downstream of the blind tee is dominated by a combined forced and free vortex, which can be approximated by Rankine's Compound Vortex model (Katopodes, 2019). In addition, the tangential velocity of the base vortex is an order of magnitude higher than that of the outer- and inner-side vortices, implying that the base vortex generates most of the tangential momentum in the blind-tee pipe.

The swirl number S is used by many scholars to evaluate the intensity of the vortex (Seibold et al., 2022; Sheen et al., 1996; Steenbergen & Voskamp, 1998), which is defined as the ratio of axial flux of angular momentum to the axial momentum flux as follows.

$$S = \int_0^{D/2} 2UVr^2 dr/D \int_0^{D/2} U^2 r dr \qquad (4)$$

where U represents the axial velocity, V represents the tangential velocity, and D represents the diameter of pipe.

In this section, the local swirl number S_L (i.e. the integral region is the vortex area) is adopted to quantify the intensities of different types of vortices, and the global swirl number S_G (i.e. the integral region is the whole cross section, which is widely used by many researchers) is used to evaluate the cross-sectional vortex strength and its attenuation along the pipe. The local swirl numbers S_L of the base vortex, inner-side vortex and outer-side vortex at $x/D = 1.3$ are displayed in Figure 10(a). Similar to the previous discussion, S_L of the base vortex is much higher than that of inner- and outer-side vortices, indicating that the base vortex is the main source of the tangential motion in blind-tee pipe. Then, the global swirl numbers S_G on different sections downstream of the blind tee (i.e. $x/D = 0.5, 0.8, 1, 1.3, 1.5, 2.5, 3.5, 4.5$ and 5.5) are shown in Figure 10(b). The value of S_G at the exit of the blind section (i.e. $x/D = 0.5$) is 0.478 for this specific structure, which is only 0.112 in the traditional elbow at the same flow condition. It reveals that the vortex strength generated by the blind tee is three times higher than that of the traditional elbow. In addition, it can be observed that the value of S_G decreases by more than 50% in the first $1D$ length downstream of the blind section (i.e. $0.5 < x/D < 1.5$), and then decreases much slower at $x/D \geq 1.5$. The backflow is considered to be the main reason for the high S_G value at the exit of the blind section and the high decline rate of S_G in the range of $0.5 < x/D < 1.5$
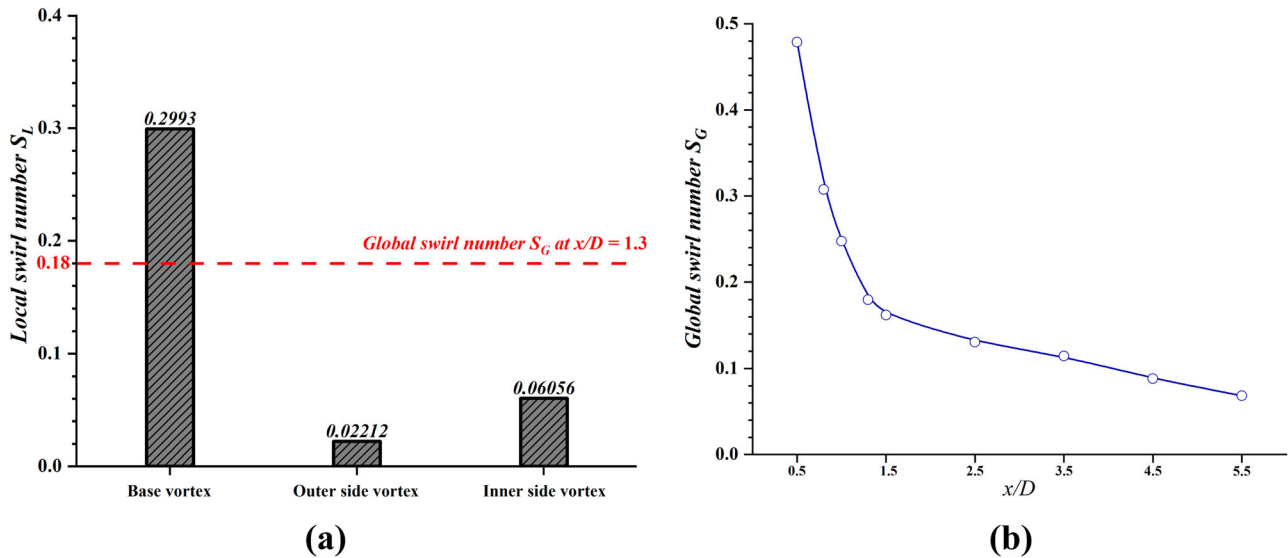
Figure 10. Swirling strengths of blind tee with BSL $= 2D$ at $Re = 1000$: (a) Local swirl number S_L of base vortex, inner-side vortex and outer-side vortex at $x/D = 1.3$; (b) Global swirl number S_G downstream of the blind section.

since it generates a strong vortex flow in the blind section and promote the mixing with the main flow in the downstream of the blind tee as shown in Figure 7. According to the above discussion, the pair of base vortices dominates the fluid mixing process in the downstream pipe, and the backflow plays an important role in the improvement of vortex strength for the secondary flow downstream of the blind tee.

Next, the influences of the blind-tee length and Reynolds numbers on the vortex generation in blind-tee pipes are discussed. Many researchers have analyzed the generation of extra vortices (i.e. the Dean vortex development from two-vortex to four-vortex or even from four-vortex to six-vortex) in curved pipes in the laminar flow regime (Dennis & Ng, 1982; Nandakumar & Masliyah, 1982). Yanase et al. (1994) defined the critical Reynolds number to reveal the generation of extra vortices in bending structures, and pointed out that the appearances of these extra vortices are mainly caused by both the convective effect and strong centrifugal force at low Reynolds numbers. In order to discuss the development of secondary flow downstream of the blind section, the vortex structures in the blind tees with BSL ranging from 1D to 3D are analyzed in Figures 11 and 12 with the Reynolds numbers varying from 500 to 1500. The first and second critical Reynolds numbers are employed to reveal the appearance of outer-side vortices and the splits of base vortex cores in the downstream pipe, respectively.

Since the inner- and outer-side vortices firstly appear at the position of $x/D = 1.3$, Figure 11 shows the variation of secondary flow structures on this section in the blind tee with BSL $= 2D$ under different Reynolds numbers. There are only two pairs of vortices (i.e. the base

and inner-side vortices) downstream of the blind tee at $Re = 500$ and 600. When the Reynolds number increases to 700, the outer-side vortices appear and become larger with the increase of Reynolds number. Therefore, $Re = 700$ is considered as the first critical Reynolds number indicating the generation of additional vortices in the bending structure. As the Reynolds number continues to increase, the core of the base vortex splits into two small vortices at $Re = 1100$, which is considered as the second critical Reynolds number, and the outer-side vortices develop from the centreline to the side walls.

In addition, the secondary flow structures in blind tees with BSL $= 1D$ and $3D$ have been discussed in Figure 12. It can be found that the first critical Reynolds number Re_{c1} is always 700 regardless of the blind-section length, and the secondary flow structure almost stays the same in different blind tees when Re is lower than 700. However, the second critical Reynold number Re_{c2} increases with the increase of blind-section length, the values of which for BSL $= 1D$, $2D$ and $3D$ are 900, 1100 and 1500, respectively. Therefore, it can be inferred that the generation of extra vortex at the first critical Reynolds number is mainly due to the centrifugal force and weakly related to the blind-tee length. However, the second critical Reynolds number is considered to be relevant to the blind-tee effect. When the Reynolds number exceeds Re_{c2}, the base vortices split, and four pairs of vortices generate to form a multidirectional fluid exchange condition at $x/D = 1.3$. Multiple pairs of vortices can stretch the fluid interface, increase the magnitudes of gradients normal to the interface, and promote the contact of different portions, by means of which the fluid mixing is enhanced downstream of the blind tee. The variation
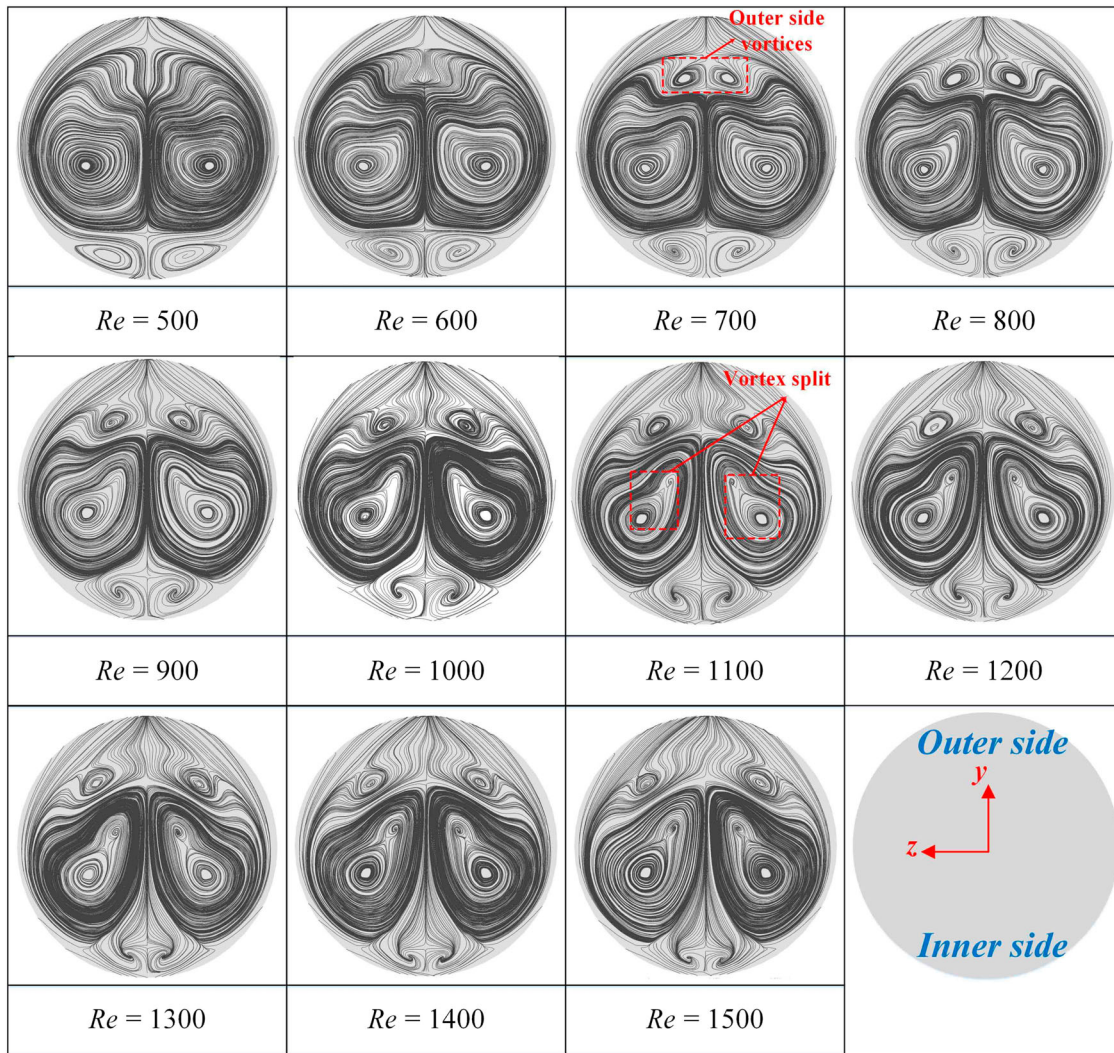
Figure 11. Secondary flow structures at $x/D = 1.3$ in blind tee with BSL $= 2D$ under different Reynolds numbers.

of Re_{c2} with the length of blind section also implies that the blind-tee structure has a significant influence on the multi-vortex formation in the downstream pipe. To summarize, in the laminar flow regime, the blind-tee effect is quite weak when the Reynolds number is less than 700, but the blind-tee structure can significantly strengthen the fluid mixing by generating multiple pairs of vortices at a higher Reynolds number, especially when $Re \geq Re_{c2}$.

4.1.3. Vorticity dissipation downstream of blind section

The vorticity dissipation downstream of bending structures is quite important for the site selection of flowmeters. For the laminar flow in curved pipes, Jarrahi et al. (2010) recommended the cross-sectional average value of absolute axial vorticity to quantify the secondary flow intensity and fluid mixing condition, which can be defined as follows for the specific structure in this

research:

$$\zeta = \iint\limits_{S} |\partial w/\partial y - \partial v/\partial z| \qquad (5)$$

where the symbol S represents the cross-sectional area, the symbol w represents the velocity component in the z direction, and v represents the velocity component in the y direction.

The cross-sectional vorticities are extracted from the numerical results along the outlet pipe every $1D$ length, and the corresponding ζ is calculated to evaluate the vorticity dissipation and fluid mixing condition downstream of the blind section. Figure 13 shows the variations of the cross-sectional average vorticities in the $30D$ outlet pipe downstream of the bind sections with BSL $= 1D$, $2D$ and $3D$ at $Re = 500$, 1000 and 1500. The X-axis represents the dimensionless downstream distance d/D, where d is the distance from the exit of the blind section (i.e. $x/D = 0.5$) to the selected downstream cross section

and D is the pipe diameter. In order to figure out the common pattern of the vorticity dissipations in different structures and Reynolds numbers, all the ζ values are normalized by the corresponding average vorticity ζ_0 at the exit of the blind section. It can be found that, at a certain Reynolds number, the vorticity dissipations of the downstream secondary flows have a similar trend in the blind tees with different lengths. However, with the increase of the Reynolds number, the dissipation rate slows down, especially in the range of $3 \leq d/D \leq 10$. According to Figure 6, the uniform velocity profile is obtained at $x/D = 5.5$ at $Re = 1000$, indicating that the fluid is fully mixed when ζ in the outlet pipe decreases to around 20% of ζ_0, i.e. the normalized vorticity is 0.2. Thus, it can be implied that the fully mixed flow condition at $Re = 500$ and 1500 will appear around at $d/D = 3$ and 6.5, respectively. This means that the influence of

blind tee on the downstream flow is stronger in a longer distance under a high Reynolds number, but it will disappear in a short distance at low Reynolds numbers, which is quite meaningful for the site selection of flowmeters.

Many studies have proved that the vorticity dissipation of secondary flows downstream of the elbows is exponential (Kim et al., 2014; Kitoh, 1991; Kreith & Sonju, 1965; Sudo et al., 1998). Different from the flow pattern in traditional elbows, the normalized vorticity in the outlet pipe of blind tee rapidly decreases from 1 to less than 0.4 when the downstream distance increases to $d/D = 2$, and then exponentially reduces with the increase of d. The backflow from the blind section and its effect on the main flow are considered as a probable reason for the rapid dissipation of secondary flow vorticity in the range of $0 \leq d/D \leq 2$. As the downstream distance increases, the effect of backflow is weakened,
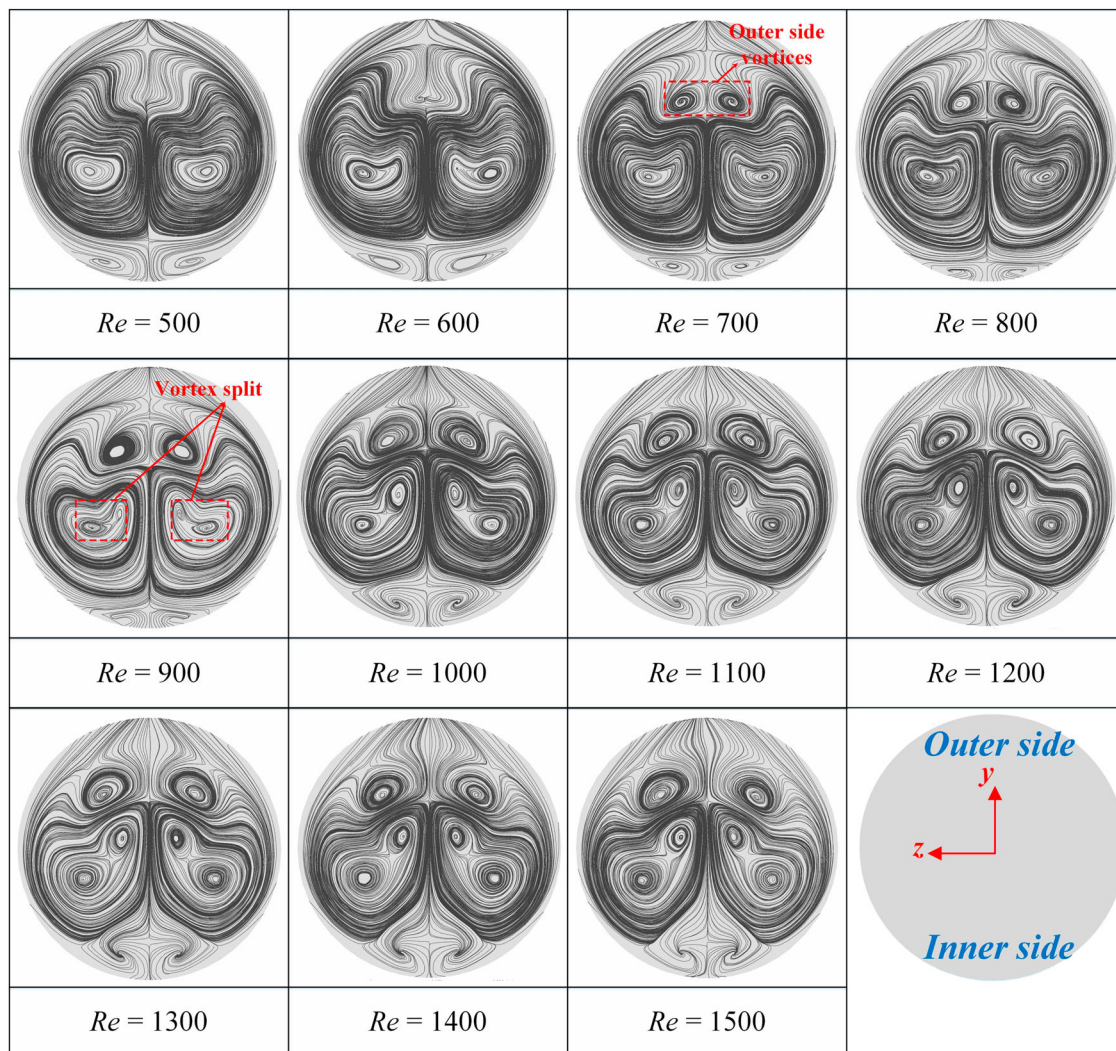
(a)

Figure 12. Secondary flow structures at $x/D = 1.3$ in blind tees with (a) BSL $= 1D$ and (b) BSL $= 3D$ under different Reynolds numbers.
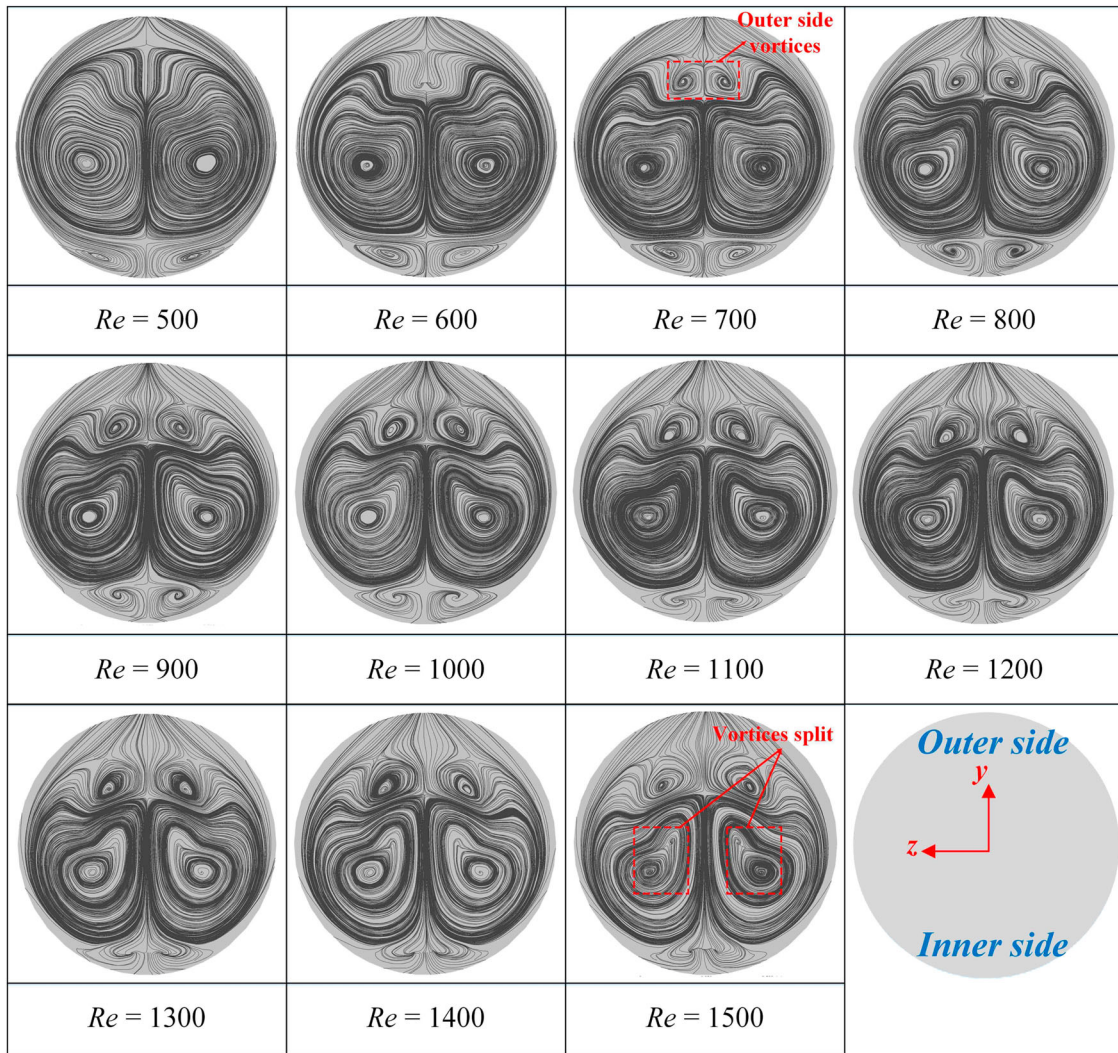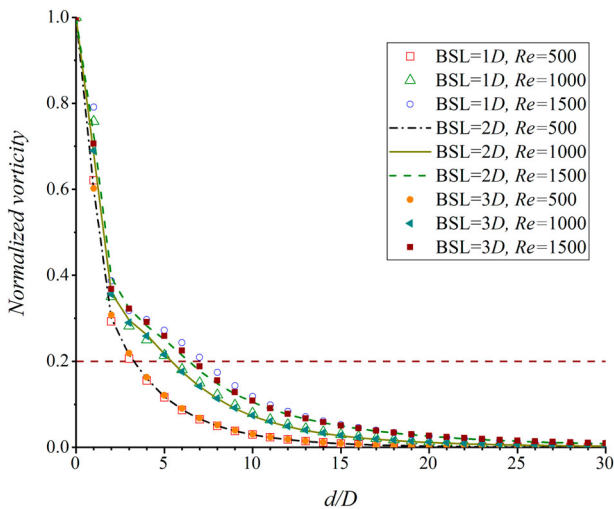
(b)

Figure 12. Continued.

Figure 13. Vorticity dissipations downstream of blind sections with BSL = 1*D*, 2*D* and 3*D* under different Reynold numbers.

and the wall friction becomes the main cause of the vorticity dissipation, resulting in an exponential dissipation curve. In order to quantify the vorticity dissipation of secondary flow in blind-tee pipes, the Levenberg-Marquardt method (Levenberg, 1944; Marquardt, 1963) is used to fit the dissipation trend of the normalized cross-sectional average vorticity, and all the coefficients of determination are higher than 0.99 in the fitting. The fitted dissipation curve of the normalized vorticity can be expressed as:

$$\zeta/\zeta_0 = \begin{cases} -\beta_1 \cdot d/D + 1, & d/D \leq 2 \\ \exp(-\beta_2 \cdot d/D)/2, & d/D > 2 \end{cases} \quad (6)$$

where β_1 and β_2 are the dissipation coefficients related to the Reynolds number, similar to the dissipation rate proposed by Kim et al. (2014).

All the dissipation coefficients for Reynolds numbers varying from 500 to 1500 have been obtained as shown in Table 1, which are expected to provide guidance for the

Table 1. Vorticity dissipation coefficients at different Reynolds numbers.

Dissipation coefficient	Reynolds number										
	500	600	700	800	900	1000	1100	1200	1300	1400	1500
β_1	0.360	0.350	0.342	0.335	0.330	0.325	0.321	0.318	0.315	0.313	0.311
β_2	0.290	0.254	0.228	0.209	0.193	0.179	0.168	0.158	0.150	0.144	0.139

site selection of flowmeters and the design of sampling schemes.
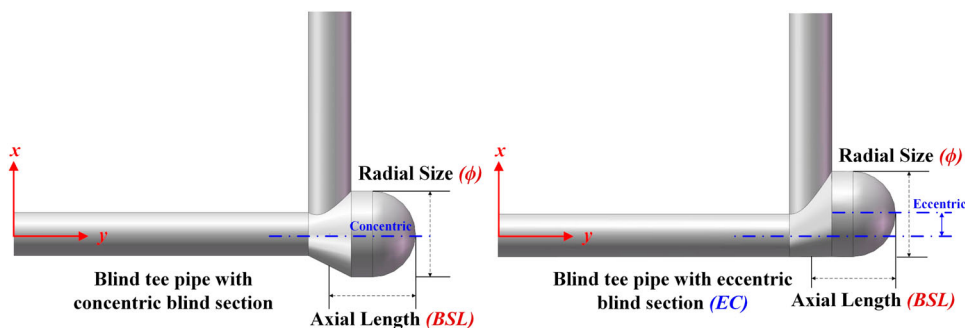
4.2. Effects of blind-tee structures

In this section, the geometrical parameters that define the blind-tee structures are systematically changed, and their effects on the pipe flow characteristics and mixing conditions are analyzed to provide references for the optimization design of blind tees. These geometrical parameters include the axial length (BSL), radial size (ϕ) and position (i.e. concentric or eccentric) of the blind section. The definitions of BSL and ϕ can be clearly observed in Figure 14. In terms of the position of blind section, the structure on the right side is the blind-tee pipe with eccentric blind section (EC), which represents that the centers of the blind section and the inlet pipe do not coincide but the bottom of the blind section is tangent to the bottom of the inlet pipe. The structure on the left side represents a normal position of blind section, i.e. the center of the blind section is concentric to the inlet pipe. For simplicity, the computational cases in this section are named with the above three geometrical parameters. For instance, BSL2D-ϕ1.5D represents the blind-tee structure with BSL $= 2D, \phi = 1.5D$ and a blind section concentric to the inlet pipe. Similarly, BSL2D-ϕ1.5D-Ec has the same axial length and radial size as BSL2D-ϕ1.5D, but the blind section is eccentric to the pipe center. Instead of the traditional flat end, the hemispherical end is adopted for all blind-tee structures proposed in this section in order to further improve the flow condition in the blind section. Numerical simulations for different blind tees analyzed in this section are carried out at $Re = 1000$.

4.2.1. Effect of radial size

Generally, the radial size ϕ of the blind section equals to the pipe diameter D. In order to study the effects of blind sections with different radial sizes on the internal flow characteristics, three-dimensional investigations have been conducted on the blind tees with enlarged blind sections, i.e. $\phi = 1.5D$ and $2D$. The results of BSL2D-ϕ1.5D and BSL2D-ϕ2D are displayed and analyzed in this part.

The two- and three-dimensional streamlines in these two configurations are shown in Figure 15. Similar flow behaviors can be found in both the regular and enlarged structures. The fluid on the upper side of the pipe turns directly to the downstream, and the fluid on the lower side enters the blind section and forms a flow circulation. Compared to the streamlines in the typical blind tee in Figure 5, the strength of the flow circulation in the blind section is enhanced in BSL2D-ϕ1.5D with higher velocities, especially at the blind end, inferring a better fluid mixing and exchanging condition of the backflow. However, in BSL2D-ϕ2D, the flow circulation becomes larger with much lower velocities in the central part of the blind tee. As a result, the fluid near the core of the circulation is almost trapped in the center of blind section, which significantly blocks the backflow passage from the blind section to the downstream pipe.

In order to develop a deeper understanding on the flow details in the blind sections of BSL2D-ϕ1.5D and BSL2D-ϕ2D, the backflows from the blind tees are shown in Figure 16 as well as the corresponding velocity vectors and contours on the cross section of $y/D = 21$. It can be observed that the backflows from the enlarged blind sections have higher velocities than that of the typical blind tee, which could enhance the mixing strength of

Figure 14. Different structures and variable geometrical parameters of blind tees.
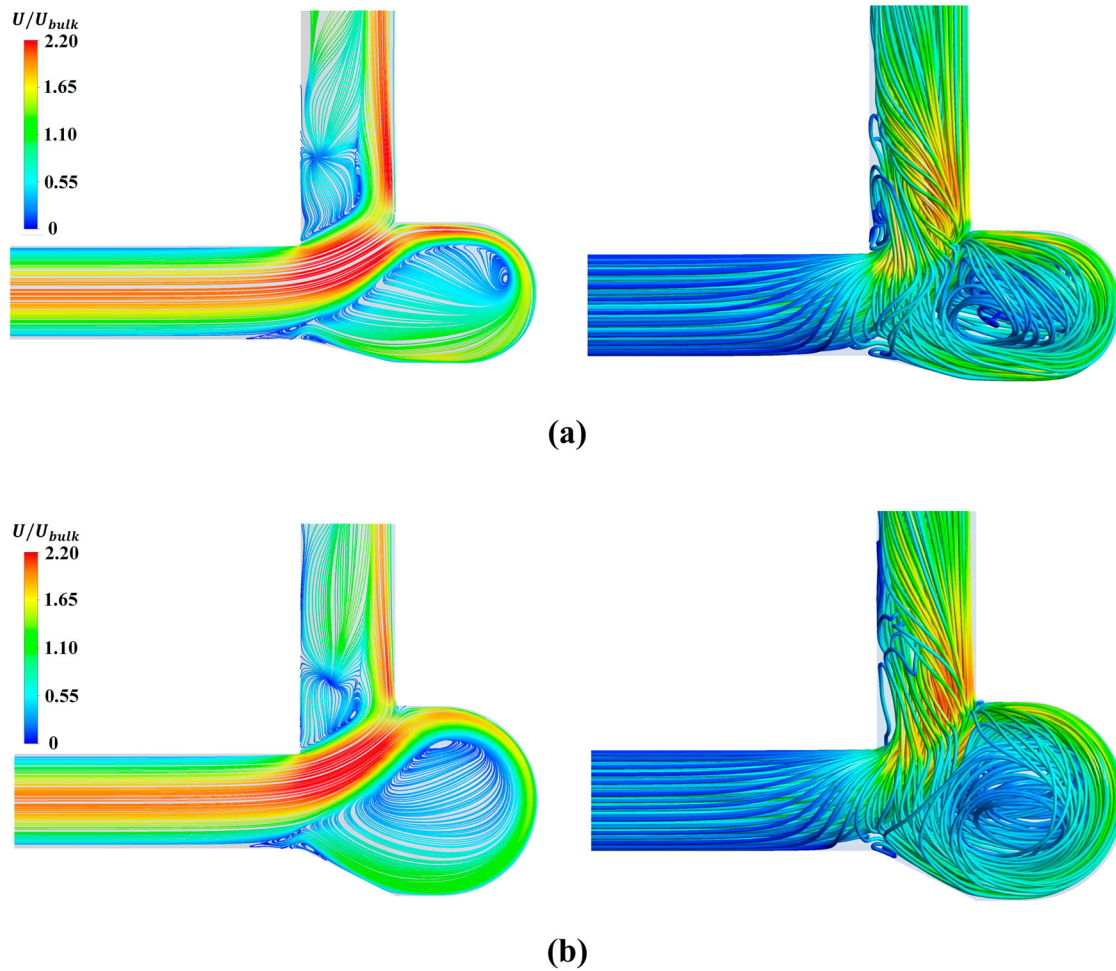
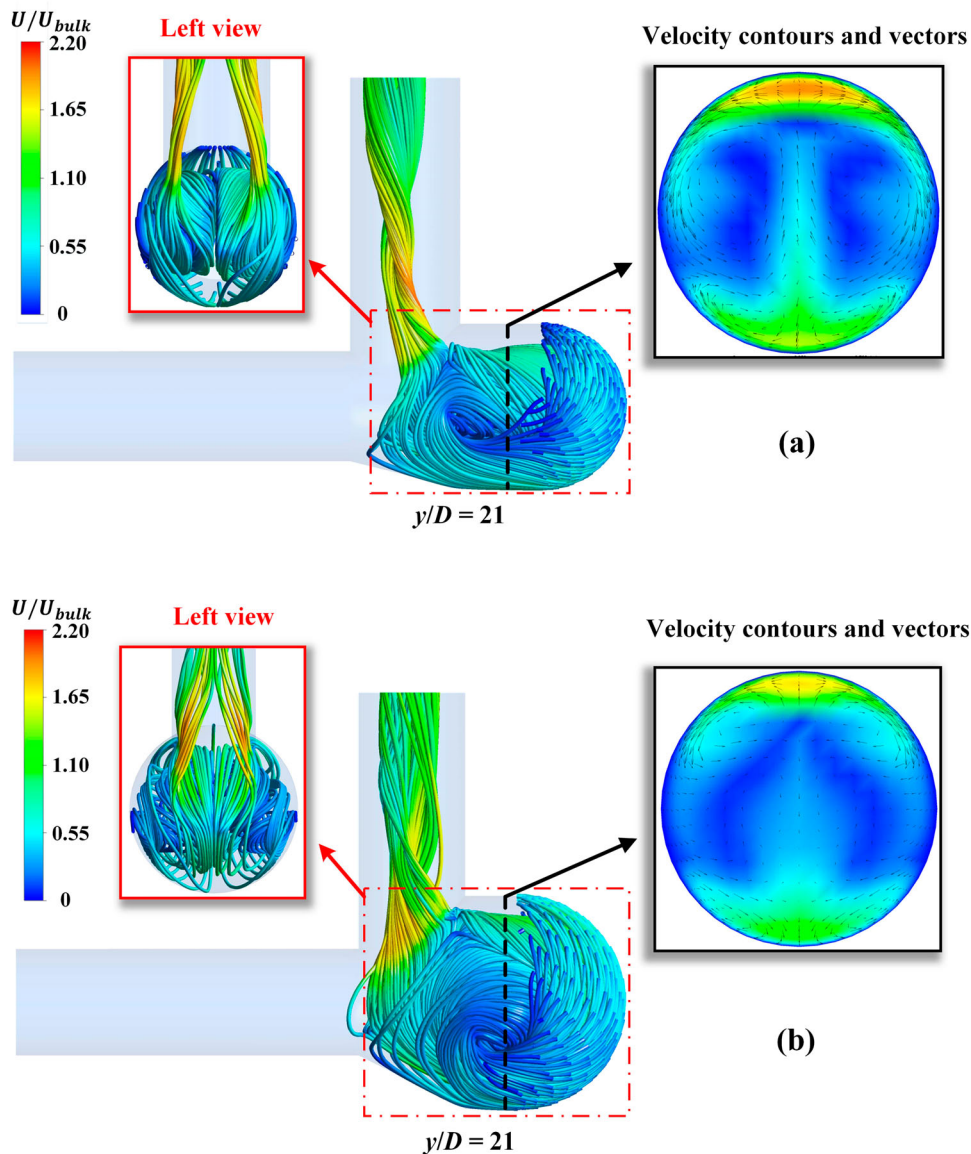**Figure 15.** Two- and three-dimensional streamlines in (a) BSL2D-ϕ1.5D and (b) BSL2D-ϕ2D.

the backflow and main flow. In addition, according to the vectors and contours on the cross section of $y/D = 21$, the velocities in the center are quite low in BSL2D-ϕ2D, and the tangential vectors there are close to zero. It indicates that the flow in the central part of blind section is almost stagnant in BSL2D-ϕ2D, and the fluid can only flow through the top and bottom regions. However, a pair of counter rotating vortices can be clearly observed in the center of the cross section in BSL2D-ϕ1.5D, revealing a good mixing condition of secondary flows in this blind section. The detailed comparisons indicate that a larger radial size will strengthen the flow circulation in a certain range, which could promote the fluid mixing and exchange between the backflow and main flow. However, with the continuous increase of the radial size, the overextended flow circulation in the blind tee may be weakened and block the fluid exchange between the blind section and the downstream pipe.

4.2.2. Effect of axial length
In this section, the axial length of the enlarged blind section with $\phi = 1.5D$ varying from $1.25D$ to $4D$

is investigated in order to reveal its influence on the flow physics in the blind tees. The two- and three-dimensional streamlines in BSL1.25D-ϕ1.5D, BSL3D-ϕ1.5D and BSL4D-ϕ1.5D are displayed in Figure 17. The flow characteristics in the configurations with variable axial lengths have significant differences. It can be observed in BSL1.25D-ϕ1.5D that the fluid flows along the end wall to form a large flow circulation, and a stagnant flow appears in the center of the blind section, which is similar to the flow pattern in BSL2D-ϕ2D shown in Figure 15(b). According to the two-dimensional streamlines, the flow separation area downstream of this blind tee is much larger than other structures. As the axial length increases to $2D$ (i.e. BSL2D-ϕ1.5D), Figure 15(a) shows that the flow separation region in the downstream pipe reduces, and the velocities of flow circulation in the blind section become much higher, which provides a better fluid exchange condition. It is also observed that the backflow streamlines flows to the downstream with a great tangential velocity, which will improve the fluid mixing across the passage downstream of the blind tee. It appears that the tangential velocity of backflow is related
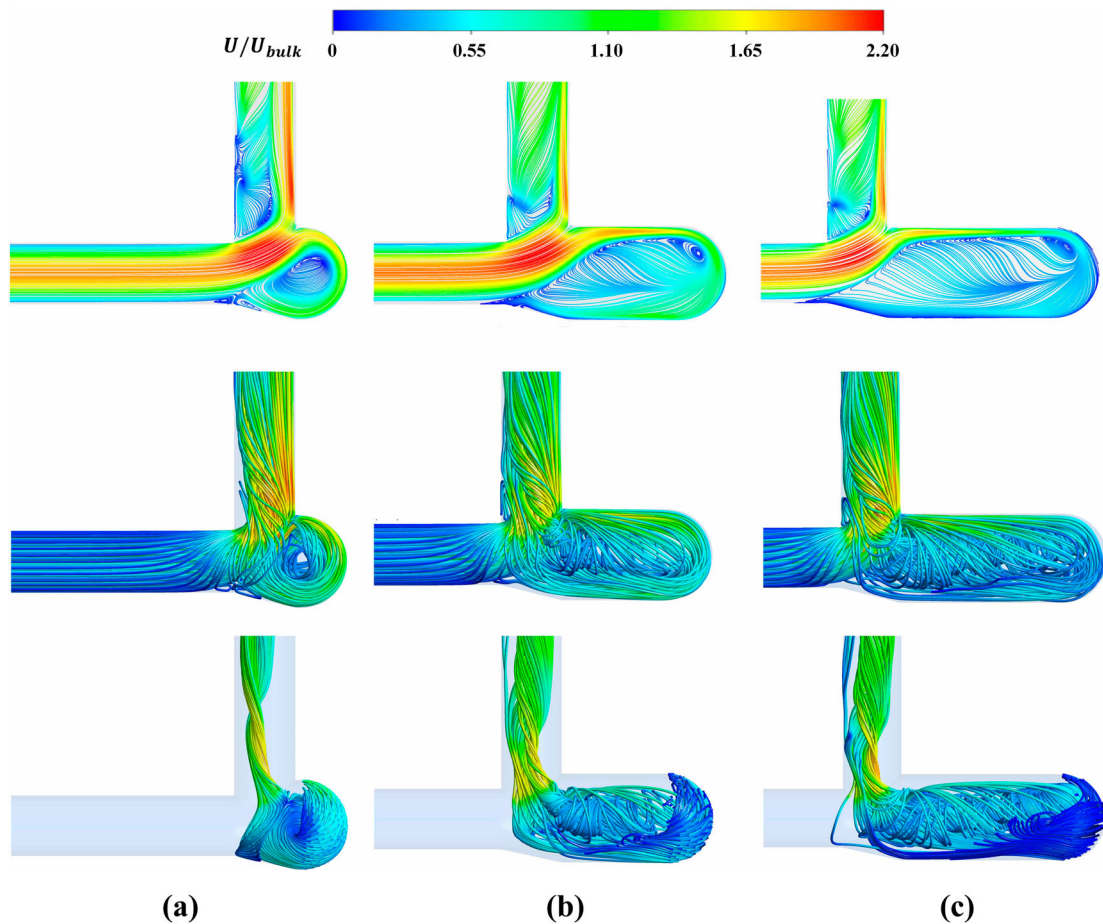
Figure 16. Three-dimensional streamlines of backflows and velocity contours in (a) BSL2D-ϕ1.5D and (b) BSL2D-ϕ2D.

to the strength of flow circulation inside the blind section. When the axial length continues to increase, the flow velocity in the blind section begins to decrease, implying a decrease in the flow circulation intensity. In addition, Figure 17(b) and (c) indicate that the backflow from the end of blind section is divided into two parts in BSL3D-ϕ1.5D and BSL4D-ϕ1.5D. Part of the fluid forms the flow circulation in the blind section, and the rest flows along the bottom of the blind tee with a very low speed, which may induce more fluid deposition in the blind section.

According to the above analysis, there are three major types of flow structures inside the blind tees with variable geometric parameters. When the ratio of the axial length to the radial size is not more than 1 (e.g. BSL1.25D-ϕ1.5D and BSL2D-ϕ2D), a large circulating flow forms in the

blind section, but more stagnant fluid appears in the center of the blind tee. As the aspect ratio increases, the flow separation range in the downstream pipe reduces, and the circulation intensity in the blind section increases, providing a better fluid exchange condition. The circulating flow in the blind section of BSL2D-ϕ1.5D is stronger than the other cases. However, as the ratio of BSL to ϕ increases to 2 or even higher (e.g. BSL3D-ϕ1.5D and BSL4D-ϕ1.5D), the backflow from the end of blind section is divided into two parts, and the low-speed part at the bottom is more likely to cause fluid depositions in the blind section. It can be concluded that a proper axial length can promote the development of flow circulation formed in the blind tee and enhance the fluid exchange between the backflow and main flow. However, the positive effect of enlarged blind section on the flow mixing

Figure 17. Two- and three-dimensional streamlines in (a) BSL1.25D-φ1.5D, (b) BSL3D-φ1.5D and (c) BSL4D-φ1.5D.

condition will be weakened by an excessive axial length. Therefore, there is an optimal value for the aspect ratio BSL/ϕ in the blind tee design, which is 1.33 for the cases analyzed in this study.

4.2.3. Effect of blind-section position

In this section, numerical simulations are performed on the blind-tee pipes with concentric and eccentric blind sections to discuss the effect of blind-tee positions. As a comparison for BSL2D-φ2D with a concentric blind section in Figure 15(b), the two- and three-dimensional flow characteristics in an eccentric blind section with the same geometric parameters (i.e. BSL2D-φ2D-Ec) are displayed in Figure 18. Great differences can be found in the flow patterns between the concentric and eccentric blind sections. As shown in the two-dimensional streamlines, instead of directly turning to the downstream from the inlet pipe, the main flow enters the blind section, and divides into two parts at the end of the structure. Part of the fluid flows along the bottom of the section and forms a small stagnant region after hitting the dead end, while most of the fluid flows directly to the blind end and reverses to the downstream along the end wall. Due

to the large centrifugal force generated by the main flow passing through the blind end, another fluid stagnation is formed in the central part of the blind tee. In addition, it can be observed that the velocity distribution downstream of the eccentric blind section is opposite to that of the concentric blind section. Since the main flow turns to the downstream from the blind section, the flow separation is formed near the outer corner of the bending structure in BSL2D-φ2D-Ec rather than near the inner corner in BSL2D-φ2D. Therefore, the high-velocity area appears on the inner side downstream of the blind tee, and the low-velocity area is near the outer side in Figure 18, which is contrary to the results of concentric blind tees.

The three-dimensional velocity vectors on the cross section of the blind-tee center (i.e. $y/D = 21$) in BSL2D-φ2D and BSL2D-φ2D-Ec are shown in Figure 19. The velocity vectors clearly indicate that the directions of flow circulations in the concentric and eccentric blind sections are opposite. The fluid flows clockwise along the end wall of the blind tee in BSL2D-φ2D, while the fluid flows through the blind section in the counter clockwise direction in BSL2D-φ2D-Ec. Furthermore, the direction
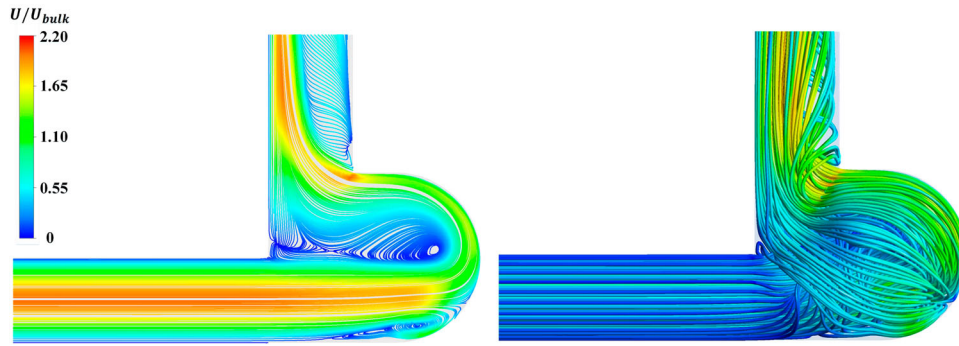
Figure 18. Two- and three-dimensional streamlines in BSL2D-φ2D-Ec.
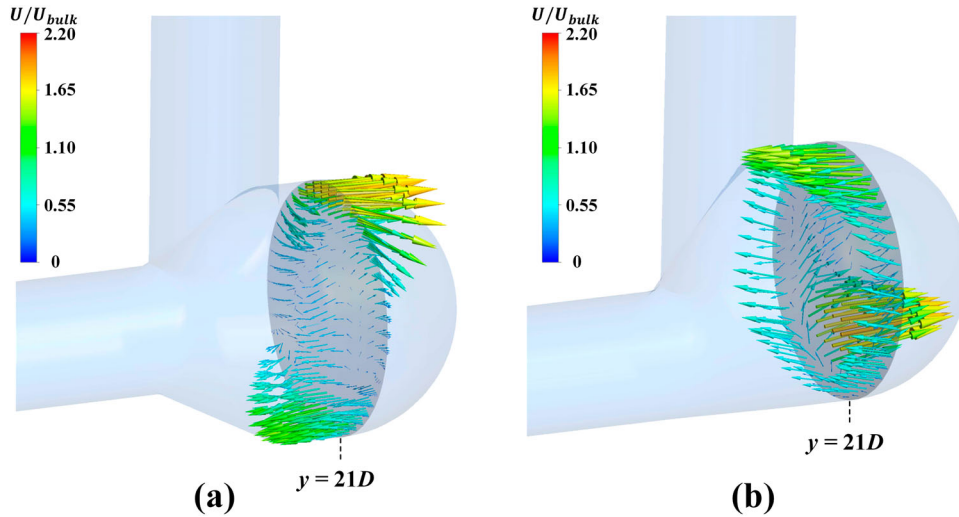
Figure 19. Three-dimensional velocity vectors on the cross section of blind tee in (a) BSL2D-φ2D and (b) BSL2D-φ2D-Ec.

of the main flow has been reversed by the end wall in BSL2D-φ2D-Ec, and an annular reversed flow area can be found along the side wall of the blind tee. From the above discussion, it can be concluded that the concentric and eccentric structures of blind tees have different mechanisms in improving the downstream flow mixing conditions. For the concentric configuration, part of the incoming fluid enters the blind tee, circulates inside the blind section, and finally flows out as the backflow to mix with the main flow. However, the eccentric configuration changes the flow path of the mainstream, and results in a flow redistribution not only inside the blind section but also in the downstream pipe, by means of which different parts of the mainstream can be mixed more effectively compared to the traditional elbows.

### 4.2.4. Mixing conditions in different structures

The purpose of this section is to compare and quantify the flow mixing conditions in various configurations of blind tees discussed in the previous sections. First, the three-dimensional vortex structures inside the six structures of blind tees are presented in Figure 20. The vortex

structures of BSL2D-φ1.5D, BSL2D-φ2D, BSL2D-φ2D-Ec, BSL1.25D-φ1.5D, BSL3D-φ1.5D and BSL4D-φ1.5D are identified by the Q-criterion (Hunt et al., 1988), which is defined as:

$$Q = (\boldsymbol{\Omega}^2 - \boldsymbol{S}^2)/2 \qquad (7)$$

where $\boldsymbol{\Omega}$ is the anti-symmetric part of the velocity gradient tensor, and $\boldsymbol{S}$ is the symmetric part.

The iso-surfaces of the nondimensionalized value $Q^* = QD^2/U_{bulk}^2 = 1.55$ are colored by the dimensionless velocity in the figure. It can be observed in Figure 20(a) and (b) that the vortex structures cover most of the surfaces in the enlarged blind sections with BSL = 2D. The vortex in blind section of BSL2D-φ1.5D is connected to other vortices in the downstream, while the vortex in BSL2D-φ2D seems to be isolated in the blind tee. This phenomenon indicates that the fluid exchange condition between the blind section and the downstream pipe is better in BSL2D-φ1.5D than in BSL2D-φ2D. It further proves that an excessive radial size of blind section is not conductive to the fluid mixing in blind tee. By comparing Figure 20(b) and (c), it can be found that the vortex structures in BSL2D-φ2D-Ec are quite different
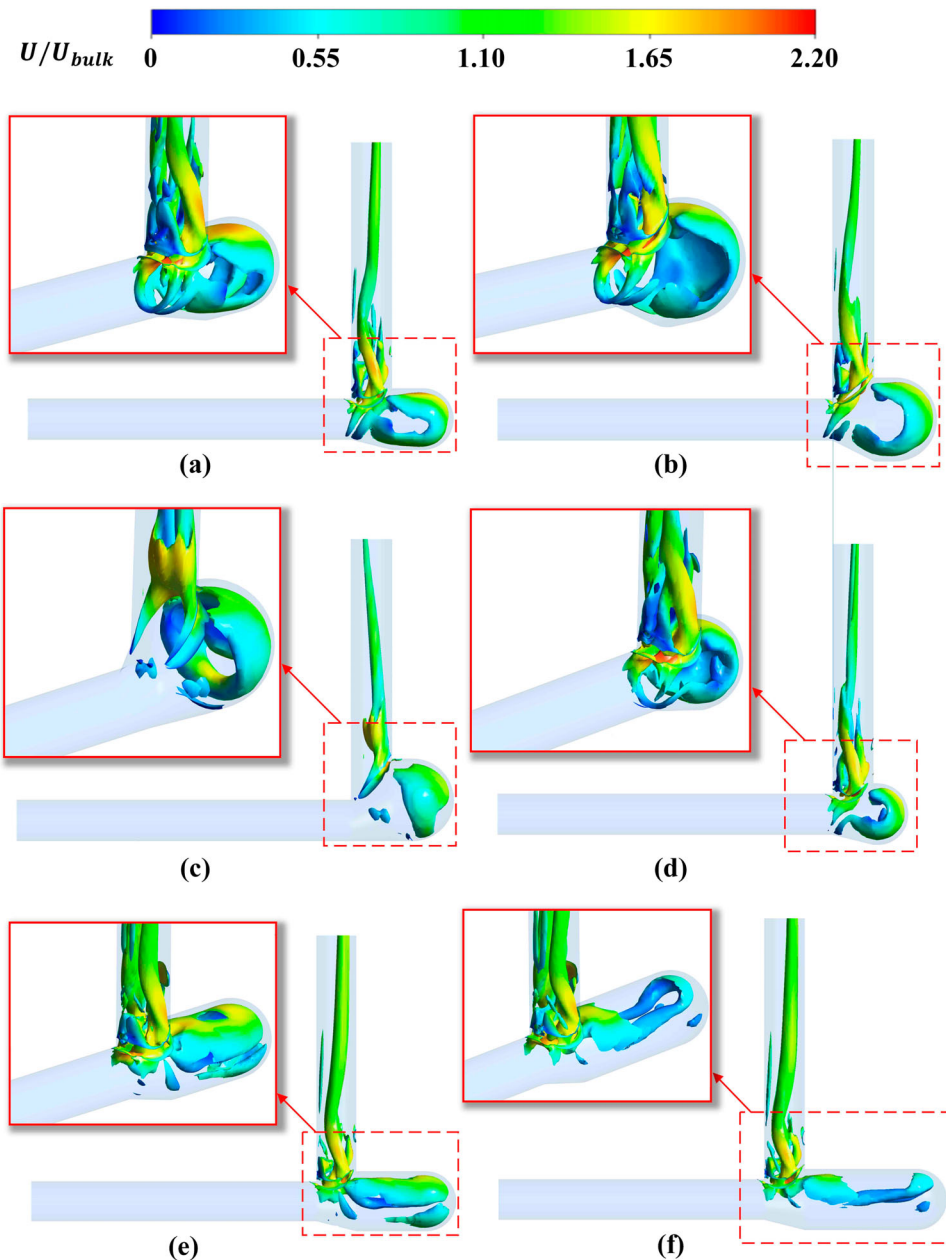
Figure 20. Three-dimensional vortex structures in (a) BSL2D-φ1.5D, (b) BSL2D-φ2D, (c) BSL2D-φ2D-Ec, (d) BSL1.25D-φ1.5D, (e) BSL3D-φ1.5D and (f) BSL4D-φ1.5D at $Q^* = 1.55$.

with that in BSL2D-φ2D, the annular vortex structures can be observed in BSL2D-φ2D-Ec. In addition, the vortex structures downstream of the eccentric and concentric blind tees are opposite. It also reveals that the flow behavior and mixing mechanism are different between the concentric and eccentric blind-tee structures.

Figure 20(d)–(f) show the variation of vortex structures with the axial length of enlarged blind sections. The vortex in the blind section of BSL1.25D-φ1.5D encircles the blind end and is isolated from the downstream vortices, just like that in BSL2D-φ2D. As the axial length increases to 3*D*, vortex structures are found only on the

upper side of the blind section, revealing that the mixing condition in blind section is weakened in BSL3D-φ1.5D. Moreover, when the axial length is increased to 4*D*, only a horseshoe vortex is found in the blind tee in Figure 20(f), implying a poor mixing condition in the blind section of BSL4D-φ1.5D. It seems that the vortex intensity in the blind section decreases with the increase of axial length. However, by comparing Figure 20(a) and (d), it can be found that the vortex in the blind section of BSL2D-φ1.5D has a larger size with higher velocities than that in BSL1.25D-φ1.5D. Therefore, the axial length of blind section has an optimal value. To sum up, the

vortex structures in different configurations are determined by the axial length, radial size and position of the blind section. When the ratio of the axial length to radial size is around 1, vortex structures surrounding the blind section can be observed as shown in Figure 20(a), (b) and (d). When the ratio increases to 2, the vortex in the blind tee is stretched and weakened, which only affects the flow on the upper side of blind section as shown in Figure 20(e) and (f). In addition, when the blind section is eccentric with the pipe center, a large annular vortex can be found at the end of blind section as shown in Figure 20(c).

In order to qualitatively evaluate the mixing conditions in the blind tees with different configurations mentioned above, the volume average vorticity Ω_{avg} is introduced to investigate the mixing capacity in the whole blind section, which is described as:

$$\Omega_{avg} = \iiint \sqrt{\begin{array}{l} (\partial w/\partial y - \partial v/\partial z)^2 \\ + (\partial u/\partial z - \partial w/\partial x)^2 \\ + (\partial v/\partial x - \partial u/\partial y)^2 \end{array}} \; d\lambda/2\lambda \quad (8)$$

where λ represents the volume of the blind section, u, v and w represent the velocities in the x, y and z directions, respectively.

Comparisons of volume average vorticities in the blind tees with different axial lengths and positions of blind section are made in Figure 21. It can be found that the vorticities in most of the modified blind tees are higher than that in the typical blind tee (i.e. BSL2D-φ1D). According to the comparison of volume vorticities in the enlarged blind sections with different axial lengths in Figure 21(a), the vorticity in the blind section increases first and then decreases with the increase of axial length, and the maximum value is achieved when the ratio of the axial length to the radial size is 1.33. The quantified result is consistent with the flow analysis in previous sections. It also reveals that, compared to the typical structure BSL2D-φ1D, the volume average vorticities in the blind sections of BSL1.25D-φ1.5D, BSL2D-φ1.5D and BSL3D-φ1.5D have increased by 42%, 53% and 20%, respectively. However, the vorticity in BSL4D-φ1.5D is 12% lower than that of the regular configuration due to the excessive axial length. In addition, the volume average vorticities in the blind sections with different radial sizes and positions are compared in Figure 21(b). It can be found that enlarging the radial size of blind section increases the volume vorticity to a certain extent, but there is also an optimal value for φ. When the radial size is increased from 1D to 1.5D, the increase of volume vorticity in the blind section is 53%. However, the volume vorticity in BSL2D-φ2D drops down to almost the same as the regular blind tee
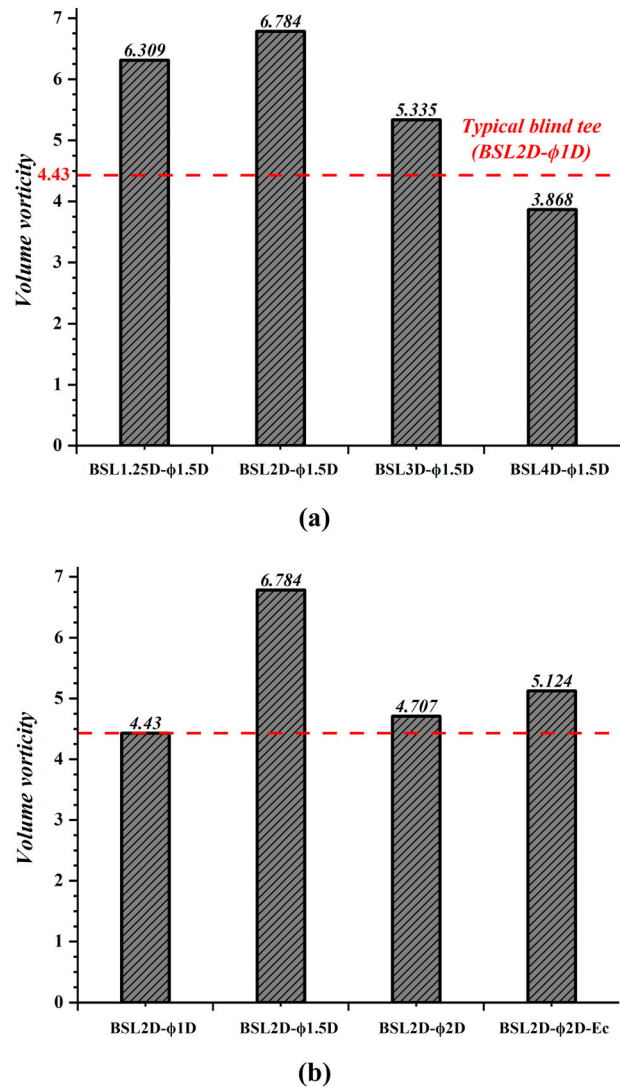
Figure 21. Comparisons of volume average vorticities in blind tees with (a) different axial lengths and (b) different radial sizes and positions of blind section.

due to the excessive radial size and overextended flow circulation. Besides, it is observed that the volume vorticity in BSL2D-φ2D-Ec is 8% higher than that of BSL2D-φ2D. This phenomenon indicates that using an eccentric blind tee can also improve the fluid mixing condition in the blind section with a larger radial size.

To summarize the analysis of the vortex structures and volume average vorticities in various blind sections, it can be concluded that increasing the radial size and axial length of the blind section in an appropriate range can significantly improve the flow mixing condition in blind-tee pipes, but an excessive increase of φ or BSL will make the vortices overextended, weakened and even disappeared. There are optimal values for these geometric parameters, and the best configuration obtained in this study is the blind tee with φ = 1.5D and BSL/φ = 1.33.

In comparison to the typical blind tee, the mixing condition in terms of volume average vorticity is improved by 53% in the optimal configuration. Additionally, compared with the concentric blind sections, the eccentric configuration can change the flow path of the mainstream and the flow patterns both inside and downstream of the blind section. As a consequence, different parts of the mainstream are fully mixed in the eccentric blind tee with an 8% increase in the volume vorticity. These results can be used as a reference for optimizing the design of blind-tee pipes for the mixing purpose.

5. Conclusions

Numerical investigations have been carried out on blind-tee pipes in order to develop an in-depth understanding of their flow mixing mechanism and clarify the effects of blind-tee structures on the pipe flow. Three-dimensional flow conditions in a typical blind tee have been simulated at different Reynolds numbers, the fluid exchange process in blind section, the blend of mainstream with backflow, the strength and development of secondary flow and the vorticity dissipation downstream of the blind section are thoroughly analyzed. Then, the geometrical parameters that define the blind-tee structures are varied systematically to investigate their effects on the pipe flow, including the radial size, axial length and position of the blind section. The flow characteristics and mixing conditions in various blind sections are qualitatively and quantitatively analyzed using the streamlines, vortex structures, velocity distributions and vorticities. The major conclusions are summarized as follows.

According to the flow analysis of the typical blind tee, there are two critical Reynolds numbers indicating the generations of extra vortices in the laminar flow regime, i.e. Re_{c1} and Re_{c2}. When $Re < Re_{c1}$, the blind tee has little effect on the downstream flow. When the Reynolds number exceeds Re_{c1}, extra vortices are generated by the centrifugal force. As the Reynolds number exceeds Re_{c2}, extra split vortices are generated by the blind tee, which greatly improve the fluid mixing condition. Moreover, the vorticity dissipation downstream of the blind section is proved to be independent of the blind-section length but related to the Reynolds number. The dissipation rate decreases with the increase of Re, and the fitting curves under different Reynolds numbers in the laminar regime are obtained to provide guidance for the site selection of flowmeters and the design of sampling schemes.

According to the structural modifications, the effects of geometrical parameters of the blind section are revealed. The results indicate that increasing the radial size and axial length of the blind section in an appropriate rang can strengthen the flow circulation in the blind tee, and promote the fluid exchange between the backflow and the mainstream. Using this method, the volume average vorticity, as a sign of the flow mixing condition in the blind tee, is increased by over 20% compared to the typical structure. However, the continuous increases of ϕ and BSL will weaken the flow circulation in the blind tee, and block the fluid exchange between the blind section and the downstream pipe. Therefore, there are optimal values for these geometric parameters. The optimal configuration obtained in this study is the blind tee with $\phi = 1.5D$ and BSL/$\phi = 1.33$, by means of which an increase up to 53% can be achieved in the mixing condition in terms of volume average vorticity. For the position of blind section, the concentric and eccentric structures of blind tees have totally different mechanisms in improving the downstream flow mixing conditions. In the eccentric configuration, the flow path of the mainstream is changed, and different parts of the main flow can be fully mixed, resulting in an 8% increase in the volume vorticity in comparison to the concentric blind tee.

This study develops an insightful understanding of the flow mechanism and mixing process in blind-tee pipes, and clarifies the influences of different geometrical parameters of blind sections on the flow characteristics. The results and new findings obtained in this paper can provide guidance and tools for the structural design and optimization of blind-tee pipes for improving the mixing conditions in further works.

ORCID

Fenghui Han ⓘ http://orcid.org/0000-0003-0061-1488
Muk Chen Ong ⓘ http://orcid.org/0000-0001-5288-5857
Guang Yin ⓘ http://orcid.org/0000-0001-8448-7183
Zhe Wang ⓘ http://orcid.org/0000-0003-4715-8510

References

Ambrose, S., Hargreaves, D. M., & Lowndes, I. S. (2016). Numerical modeling of oscillating Taylor bubbles. *Engineering Applications of Computational Fluid Mechanics*, *10*(1), 578–598. https://doi.org/10.1080/19942060.2016.1224737

Bazyleva, A. B., Hasan, M. D. A., Fulem, M., Becerra, M., & Shaw, J. M. (2010). Bitumen and heavy oil rheological properties: Reconciliation with viscosity measurements. *Journal of Chemical & Engineering Data*, *55*(3), 1389–1397. https://doi.org/10.1021/je900562u

Bhunia, A., & Chen, C. L. (2009). Flow characteristics in a curved rectangular channel with variable cross-sectional area. *Journal of Fluids Engineering*, *131*(9), 091102. https://doi.org/10.1115/1.3176970

Bovendeerd, P., Steenhoven, A., Vosse, F., & Vossers, G. (1987). Steady entry flow in a curved pipe. *Journal of Fluid Mechanics*, *177*, 233–246. https://doi.org/10.1017/S0022112087000934

Brister, C. M. (2013). *Wet gas performance of a low energy gamma ray multiphase meter*. OTC Brasil.

Cao, Y., Tamura, T., & Kawai, H. (2020). Spanwise resolution requirements for the simulation of high-reynolds-number flows past a square cylinder. *Computers & Fluids*, *196*, 104320. https://doi.org/10.1016/j.compfluid.2019.104320

Cengel, Y., & Cimbala, J. (2014). *Fluid mechanics* (3rd ed). McGraw-Hill Education.

Chacon, C., Moreno, C., Arbej, M., & Asuaje, M. (2015). *Numerical investigation of two-phase flow in 45 degrees "Y" junctions*. ASME 2015 International Mechanical Engineering Congress and Exposition.

Chen, X., McLaury, B. S., & Shirazi, S. A. (2006). Numerical and experimental investigation of the relative erosion severity between plugged tees and elbows in dilute gas/solid two-phase flow. *Wear*, *261*(7-8), 715–729. https://doi.org/10.1016/j.wear.2006.01.022

Dai, L., & Wang, X. (2014). Numerical study on mobilization of oil slugs in capillary model with level set approach. *Engineering Applications of Computational Fluid Mechanics*, *8*(3), 422–434. https://doi.org/10.1080/19942060.2014.11015526

Dean, W. R., & Chapman, S. (1928). Fluid motion in a curved channel. Proceedings of the Royal Society of London. *Series A, Containing Papers of a Mathematical and Physical Character*, *121*(787), 402–420. https://doi.org/10.1098/rspa.1928.0205

Dennis, S. C. R., & Ng, M. (1982). Dual solutions for steady laminar flow through a curved tube. *The Quarterly Journal of Mechanics and Applied Mathematics*, *35*(3), 305–324. https://doi.org/10.1093/qjmam/35.3.305

Dianita, C., Piemjaiswang, R., & Chalermsinsuwan, B. (2021). CFD simulation and statistical experimental design analysis of core annular flow in T-junction and Y-junction for oil-water system. *Chemical Engineering Research and Design*, *176*, 279–295. https://doi.org/10.1016/j.cherd.2021.10.011

Dutta, P., & Nandi, N. (2021). Numerical analysis on the development of vortex structure in 90° pipe bend. *Progress in Computational Fluid Dynamics, an International Journal*, *21*(5), 261–273. https://doi.org/10.1504/PCFD.2021.117466

Dutta, P., Saha, S. K., Nandi, N., & Pal, N. (2016). Numerical study on flow separation in 90° pipe bend under high Reynolds number by k-ϵ modelling. *Engineering Science and Technology, an International Journal*, *19*(2), 904–910. https://doi.org/10.1016/j.jestch.2015.12.005

Ebara, S., Takamura, H., Hashizume, H., & Yamano, H. (2016). Characteristics of flow field and pressure fluctuation in complex turbulent flow in the third elbow of a triple elbow piping with small curvature radius in three-dimensional layout. *International Journal of Hydrogen Energy*, *41*(17), 7139–7145. https://doi.org/10.1016/j.ijhydene.2016.02.068

Georgiou, M., & Papalexandris, M. V. (2018). Direct numerical simulation of turbulent heat transfer in a T-junction. *Journal of Fluid Mechanics*, *845*, 581–614. https://doi.org/10.1017/jfm.2018.256

Gholami, A., Akbar Akhtari, A., Minatour, Y., Bonakdari, H., & Javadi, A. A. (2014). Experimental and numerical study on velocity fields and water surface profile in a strongly-curved 90° open channel bend. *Engineering Applications of Computational Fluid Mechanics*, *8*(3), 447–461. https://doi.org/10.1080/19942060.2014.11015528

Han, F., Ong, M. C., Xing, Y., & Li, W. (2020). Three-dimensional numerical investigation of laminar flow in blind-tee pipes. *Ocean Engineering*, *217*, 107962. https://doi.org/10.1016/j.oceaneng.2020.107962

Hellström, L. H. O., Zlatinov, M. B., Cao, G., & Smits, A. J. (2013). Turbulent pipe flow downstream of a bend. *Journal of Fluid Mechanics*, *735*, Article R7. https://doi.org/10.1017/jfm.2013.534

Hjertaker, B. T., Tjugum, S. A., Hallanger, A., & Maad, R. (2018). Characterization of multiphase flow blind-T mixing using high speed gamma-ray tomometry. *Flow Measurement and Instrumentation*, *62*, 205–212. https://doi.org/10.1016/j.flowmeasinst.2017.10.001

Hunt, J. C. R., Wray, A. A., & Moin, P. (1988). *Eddies, streams, and convergence zones in turbulent flows*. Center For Turbulence Research, Report CTR-S88.

Ilyin, S. O., & Strelets, L. A. (2018). Basic fundamentals of petroleum rheology and their application for the investigation of crude oils of different natures. *Energy & Fuels*, *32*(1), 268–278. https://doi.org/10.1021/acs.energyfuels.7b03058

Jarrahi, M., Castelain, C., & Peerhossaini, H. (2010). Secondary flow patterns and mixing in laminar pulsating flow through a curved pipe. *Experiments in Fluids*, *50*(6), 1539–1558. https://doi.org/10.1007/s00348-010-1012-z

Kalpakli Vester, A., Örlü, R., & Alfredsson, P. H. (2015). POD analysis of the turbulent flow downstream a mild and sharp bend. *Experiments in Fluids*, *56*(3), 1–15. https://doi.org/10.1007/s00348-015-1926-6

Katopodes, N. D. (2019). Chapter 7 - vorticity dynamics. In N. D. Katopodes (Ed.), *Free-Surface flow* (pp. 516–565). Butterworth-Heinemann.

Keleşoğlu, S., Pettersen, B. H., & Sjöblom, J. (2012). Characterization of Water-in-North sea acidic crude oil emulsions by means of rheology, droplet size, and laminar flow in pipeline. *Journal of Dispersion Science and Technology*, *33*(4), 536–548. https://doi.org/10.1080/01932691.2011.574937

Kim, J., Yadav, M., & Kim, S. (2014). Characteristics of secondary flow induced by 90-degree elbow in turbulent pipe flow. *Engineering Applications of Computational Fluid Mechanics*, *8*(2), 229–239. https://doi.org/10.1080/19942060.2014.11015509

Kitoh, O. (1991). Experimental study of turbulent swirling flow in a straight pipe. *Journal of Fluid Mechanics*, *225*, 445–479. https://doi.org/10.1017/S0022112091002124

Komen, E., Shams, A., Camilo, L., & Koren, B. (2014). Quasi-DNS capabilities of OpenFOAM for different mesh types.

Computers & Fluids, 96, 87–104. https://doi.org/10.1016/j.compfluid.2014.02.013

Kreith, F., & Sonju, O. K. (1965). The decay of a turbulent swirl in a pipe. *Journal of Fluid Mechanics*, 22(2), 257–271. https://doi.org/10.1017/S0022112065000733

Kresta, S. M., & Wood, P. E. (1993). The flow field produced by a pitched blade turbine: Characterization of the turbulence and estimation of the dissipation rate. *Chemical Engineering Science*, 48(10), 1761–1774. https://doi.org/10.1016/0009-2509(93)80346-R

Levenberg, K. (1944). A method for the solution of certain non-linear problems in least squares. *Quarterly of Applied Mathematics*, 2(2), 164–168. https://doi.org/10.1090/qam/10666

Li, Y., Wang, X., Zhou, B., Yuan, S., & Tan, S. K. (2017). Dean instability and secondary flow structure in curved rectangular ducts. *International Journal of Heat and Fluid Flow*, 68, 189–202. https://doi.org/10.1016/j.ijheatfluidflow.2017.10.011

Lim, K. W., & Chung, M. K. (1999). Numerical investigation on the installation effects of electromagnetic flowmeter downstream of a 90° elbow-laminar flow case. *Flow Measurement and Instrumentation*, 10(3), 167–174. https://doi.org/10.1016/S0955-5986(98)00052-1

Liu, X., Gong, C., Zhang, L., Jin, H., & Wang, C. (2019). Numerical study of the hydrodynamic parameters influencing internal corrosion in pipelines for different elbow flow configurations. *Engineering Applications of Computational Fluid Mechanics*, 14(1), 122–135. https://doi.org/10.1080/19942060.2019.1678524

Liu, Y., Han, F., Zhang, H., Wang, D., Wang, Z., & Li, W. (2021). *Numerical simulation of internal flow in jumper tube with blind tee*. 2021 IEEE 16th Conference on Industrial Electronics and Applications (ICIEA).

Lv, W., Ou, G., Liu, X., & Gong, C. (2020). Experimental and numerical studies on the corrosion properties of AISI 316L stainless steel in two-phase upward slug flows. *Engineering Applications of Computational Fluid Mechanics*, 14(1), 897–909. https://doi.org/10.1080/19942060.2020.1780155

Marquardt, D. W. (1963). An algorithm for least-squares estimation of nonlinear parameters. *Journal of the Society for Industrial and Applied Mathematics*, 11(2), 431–441. https://doi.org/10.1137/0111030

Moser, R. D., & Moin, P. (1987). The effects of curvature in wall-bounded turbulent flows. *Journal of Fluid Mechanics*, 175(-1), 479–510. https://doi.org/10.1017/S0022112087000491

Nandakumar, K., & Masliyah, J. H. (1982). Bifurcation in steady laminar flow through curved tubes. *Journal of Fluid Mechanics*, 119, 475–490. https://doi.org/10.1017/S002211208200144X

Norouzi, M., & Biglari, N. (2013). An analytical solution for Dean flow in curved ducts with rectangular cross section. *Physics of Fluids*, 25(5), 053602. https://doi.org/10.1063/1.4803556

Ong, M. C., Liu, S., Liestyarini, U. C., & Xing, Y. (2017). *Three dimensional numerical simulation of flow in blind-tee pipes*. The 9th National Conference on Computational Mechanics.

Özkan, F., Wenka, A., Hansjosten, E., Pfeifer, P., & Kraushaar-Czarnetzki, B. (2015). Numerical investigation of interfacial mass transfer in two phase flows using the VOF method. *Engineering Applications of Computational Fluid Mechanics*, 10(1), 100–110. https://doi.org/10.1080/19942060.2015.1061555

Pantokratoras, A. (2016). Steady laminar flow in a 90° bend. *Advances in Mechanical Engineering*, 8(9), 1–9. https://doi.org/10.1177/1687814016669472

Pinguet, B. G., Vethe, E., Smith, M. T., Smith, G., Sbordone, A., & Nighswander, J. A. (2012). *Subsea sampling: Reducing uncertainty from PVT by utilizing representative sampling subsea*. Offshore Technology Conference.

Pouraria, H., Seo, J. K., & Paik, J. K. (2016). Numerical study of erosion in critical components of subsea pipeline: Tees vs bends. *Ships and Offshore Structures*, 12(2), 233–243. https://doi.org/10.1080/17445302.2015.1131889

Rammohan, A., Bhakta, A., Natrajan, V., Ward, J., & Kumar, M. (2013). *Flow swirl and flow profile measurement in multiphase flow*. 31st International North Sea Flow.

Razali, M. A. B., Xie, C.-G., & Loh, W. L. (2021). Experimental investigation of gas-liquid flow in a vertical venturi installed downstream of a horizontal blind tee flow conditioner and the flow regime transition. *Flow Measurement and Instrumentation*, 80, 101961. https://doi.org/10.1016/j.flowmeasinst.2021.101961

Sakowitz, A., Mihaescu, M., & Fuchs, L. (2013). Effects of velocity ratio and inflow pulsations on the flow in a T-junction by Large Eddy simulation. *Computers & Fluids*, 88, 374–385. https://doi.org/10.1016/j.compfluid.2013.10.001

Sakowitz, A., Mihaescu, M., & Fuchs, L. (2014). Turbulent flow mechanisms in mixing T-junctions by Large Eddy simulations. *International Journal of Heat and Fluid Flow*, 45, 135–146. https://doi.org/10.1016/j.ijheatfluidflow.2013.06.014

Santos, R. G. d., Brinceño, M. I., & Loh, W. (2017). Laminar pipeline flow of heavy oil–in–water emulsions produced by continuous in-line emulsification. *Journal of Petroleum Science and Engineering*, 156, 827–834. https://doi.org/10.1016/j.petrol.2017.06.061

Seibold, F., Ligrani, P., & Weigand, B. (2022). Flow and heat transfer in swirl tubes — A review. *International Journal of Heat and Mass Transfer*, 187, 122455. https://doi.org/10.1016/j.ijheatmasstransfer.2021.122455

Sheen, H. J., Chen, W. J., Jeng, S. Y., & Huang, T. L. (1996). Correlation of swirl number for a radial-type swirl generator. *Experimental Thermal and Fluid Science*, 12(4), 444–451. https://doi.org/10.1016/0894-1777(95)00135-2

Steenbergen, W., & Voskamp, J. (1998). The rate of decay of swirl in turbulent pipe flow. *Flow Measurement and Instrumentation*, 9(2), 67–78. https://doi.org/10.1016/S0955-5986(98)00016-8

Sudo, K., Sumida, M., & Hibara, H. (1998). Experimental investigation on turbulent flow in a circular-sectioned 90-degree bend. *Experiments in Fluids*, 25(1), 42–49. https://doi.org/10.1007/s003480050206

Venters, R., Helenbrook, B. T., Ahmadi, G., Bohl, D., & Bluestein, A. (2021). Flow through an elbow: A direct numerical simulation investigating turbulent flow quantities. *International Journal of Heat and Fluid Flow*, 90, 108835. https://doi.org/10.1016/j.ijheatfluidflow.2021.108835

Vittorio Messa, G., & & Malavasi, S. (2014). Numerical prediction of particle distribution of solid-liquid slurries in straight pipes and bends. *Engineering Applications of Computational Fluid Mechanics*, 8(3), 356–372. https://doi.org/10.1080/19942060.2014.11015521

Xu, H., Chen, W., & Hu, W. (2020). Hydraulic transport flow law of natural gas hydrate pipeline under marine dynamic

environment. *Engineering Applications of Computational Fluid Mechanics*, *14*(1), 507–521. https://doi.org/10.1080/19942060.2020.1727774

Yanase, S., Yamamoto, K., & Yoshida, T. (1994). Effect of curvature on dual solutions of flow through a curved circular tube. *Fluid Dynamics Research*, *13*(3-4), 217–228. https://doi.org/10.1016/0169-5983(94)90050-7

Yuki, K., Hasegawa, S., Sato, T., Hashizume, H., Aizawa, K., & Yamano, H. (2011). Matched refractive-index PIV visualization of complex flow structure in a three-dimentionally connected dual elbow. *Nuclear Engineering and Design*, *241*(11), 4544–4550. https://doi.org/10.1016/j.nucengdes.2010.12.026